Atmospheric Pollution Research 17 (2026) 103077

Contents lists available at ScienceDirect

Atmospheric Pollution Research

journal homepage: www.elsevier.com/locate/apr

PM_{10} source apportionment in a coastal african megacity (Luanda, Angola): A quantitative basis for air quality management

Alan Victor da Silva [a,*], Yago Cipoli [a], Estela Vicente [a], Ana Sanchez de la Campa [b], Anabela Leitão [c], Manuel Feliciano [d], Célia Alves [a,**]

[a] Department of Environment and Planning, CESAM — Centre for Environmental and Marine Studies, University of Aveiro, Aveiro, 3810-193, Portugal
[b] Associate Unit CSIC-University of Huelva "Atmospheric Pollution", Centre for Research in Sustainable Chemistry - CIQSO, ETSI, University of Huelva, Huelva, 21071, Spain
[c] LESRA – Separation, Chemical Reaction, and Environmental Engineering Laboratory, Agostinho Neto University, Av. Ho Chi Minh n° 201, Luanda, Angola
[d] CIMO, LA SusTEC, Polytechnic Institute of Bragança, Santa Apolónia Campus, Bragança, 5300-253, Portugal

ARTICLE INFO

Keywords:
Luanda
PM_{10}
Source apportionment
Positive matrix factorisation
Industrial/metal-related sources

ABSTRACT

Urban air quality in African megacities remains under-represented in observational studies, and Luanda (Angola) is no exception, despite rapid urbanisation and evidence of high particulate levels. This study presents the first PM_{10} source apportionment for Luanda, based on daily samples collected from June to November 2023 using gravimetric samplers and chemically characterised for water-soluble ions, carbonaceous fractions, elements and levoglucosan. Sources were resolved with the Positive Matrix Factorisation model, supported by local meteorology, HYSPLIT back-trajectories and NASA FIRMS active-fire detections. Model diagnostics ($Q_{(Robust)}/Q_{(Expected)}$, residuals, Bootstrap, DISP and Fpeak) indicated a stable six-factor solution that reproduced measured PM_{10} with high agreement ($R^2 = 0.95$; RMSE = 3.95 μg m^{-3}). Traffic-related emissions dominate PM_{10} (37.6%), represented by a mixed exhaust/non-exhaust factor encompassing tailpipe emissions, brake and tyre wear, and road-dust resuspension. Metal-related industrial emissions are represented by a Zn–Pb–Cd–Sn-rich factor attributed to non-ferrous metallurgy and galvanised/electronic-scrap handling and burning (10.8%), and a Ni-centred metallurgical factor with a potential aviation influence (6.4%). Natural and geogenic sources contribute 29.6%, divided between crustal material + resuspended dust (16.5%) and marine aerosol (13.1%). A mixed secondary aerosol and biomass-burning factor (SA + BB) accounts for the remaining 15.5% and is associated with regionally transported, chemically aged plumes linked to inland fire activity. Overall, traffic and metal-related activities dominate PM_{10} in Luanda and provide a first quantitative basis for air quality management in this coastal African megacity.

1. Introduction

The State of Global Air (2025) report estimated that air pollution was responsible for 7.9 million deaths in 2023, with a disproportionate share of the burden occurring in low-income countries. In Africa alone, air pollution was associated with 1.1 million deaths. A substantial share of these impacts was attributed to exposure to particulate matter (PM), which remains the leading contributor to air pollution-related mortality (HEI, 2025). PM is, in fact, widely recognised as a major environmental risk factor for morbidity and premature mortality (Krittanawong et al., 2023; Yu et al., 2022; Zhao et al., 2025; Zheng et al., 2024). Although global burden assessments are primarily centred on $PM_{2.5}$, PM_{10} remains directly relevant to public health because it represents the inhalable particle fraction, encompassing both fine and coarse particles, and is associated with adverse cardiorespiratory outcomes. A recent systematic review and meta-analysis reported clear evidence that both $PM_{2.5}$ and PM_{10} are associated with increased mortality from all causes, cardiovascular disease, respiratory disease and lung cancer (Chen and Hoek, 2020). Direct PM_{10} health-impact assessments also indicate a substantial burden: in 13 Italian cities, PM_{10} concentrations above 20 μg m^{-3} were estimated to account for approximately 8220 deaths per year, corresponding to 9% of all-cause mortality among adults older than 30

* Corresponding author.
** Corresponding author.
E-mail addresses: alanvisi@gmail.com (A.V. da Silva), celia.alves@ua.pt (C. Alves).

https://doi.org/10.1016/j.apr.2026.103077
Received 23 February 2026; Received in revised form 25 May 2026; Accepted 25 May 2026
Available online 26 May 2026

years (Martuzzi et al., 2006).

Across Africa, air quality monitoring capacity is extremely limited and remains one of the major bottlenecks for environmental health assessment (Amegah, 2018; Malings et al., 2020). According to UNICEF's 2019 assessment, only about 6% of African children lived within 50 km of a reliable ground-level air quality monitoring station, compared with roughly 70–72% in Europe and North America (Rees et al., 2019). As a consequence, long-term trends, source contributions and spatial patterns of ambient PM remain poorly documented for most African cities. While household combustion of solid fuels has historically been the dominant exposure pathway, rapid urbanisation, increased motorisation and industrial growth have led to a marked shift towards outdoor urban pollution as a key health burden. Nevertheless, only 17 African countries have adopted national legislative air quality standards, and Angola is not among them (OECD/SWAC, 2025). This regulatory gap is particularly concerning given recent measurements indicating that PM_{10} concentrations in Luanda, a coastal megacity experiencing rapid expansion, range from 23.6 to 108 μg m^{-3} (average ~59.3 μg m^{-3}), substantially exceeding WHO guidelines and suggesting recurrent unhealthy air quality (Alves et al., 2025; da Silva et al., 2025).

The combined lack of regulatory standards, formal monitoring infrastructure and emission inventories makes it difficult to identify the major contributors to PM pollution and to design mitigation strategies that are tailored to local conditions (Fisher et al., 2021). In such contexts, quantitative source apportionment using receptor models offers a powerful and practical approach to evaluate the relative importance of different emission sources in the absence of detailed emission data. Receptor models based on multivariate statistics, especially Positive Matrix Factorisation (PMF), have been widely applied in urban environments to infer source profiles and contributions from chemically speciated PM datasets (Demir et al., 2022; Hsu et al., 2021; Ogundele et al., 2016; Srivastava et al., 2021). As a source-unknown model, PMF does not require predefined source profiles; instead, it uses covariance structures across multiple species to infer the number of sources, their characteristic chemical signatures and their temporal behaviour (Wang et al., 2025). This makes PMF particularly suitable for exploratory analyses and for settings where emission inventories are incomplete or unreliable, as is the case in many African countries.

Against this broader African context, Luanda remains a major evidence gap, although the limited available literature points to a broadly consistent source pattern. Higher pollutant concentrations have been reported at central urban locations compared to suburban areas such as Talatona, reflecting the combined influence of dense traffic and major fixed sources, including the airport, thermoelectric power plants, refinery, cement facilities, and the Port of Luanda (Campos et al., 2021). Passive monitoring across the metropolitan area similarly revealed elevated NO_2, SO_2, and aromatic volatile organic compound concentrations at traffic-influenced sites, as well as a distinct landfill-related signal at Mulenvos (Alves et al., 2024). More recent studies have further refined this picture by documenting high PM_{10} and $PM_{2.5}$ concentrations (da Silva et al., 2025) and identifying contributions from mineral dust, sea salt, traffic-related emissions (including brake and tyre wear), industrial activities, fossil fuel combustion and petroleum refining, and biomass burning (Alves et al., 2025). A similar source pattern has also been observed in school-based PM_{10} characterisation studies, despite their focus on indoor environments (Alves et al., 2026).

However, despite this emerging evidence, quantitative source-resolved information for PM_{10} in Luanda remains limited. The present study addresses this gap by applying the U.S. EPA PMF 5.0 receptor model to a chemically speciated PM_{10} dataset collected in central Luanda between June and November 2023. Beyond providing the first PM_{10} source apportionment for Luanda, this study delivers receptor-based estimates of source contributions, helps disentangle chemically overlapping sources such as traffic emissions, mineral dust and industrial activities, and evaluates the relative importance of local and transported contributions. By integrating PMF results with meteorological observations, HYSPLIT back trajectories and NASA FIRMS fire detections, this work provides source-resolved quantitative evidence to support air quality management in a data-scarce African megacity.

2. Material and methods

2.1. Sampling site and monitoring equipment

Ambient particulate matter (PM_{10}) was collected in Luanda, at the Faculty of Engineering, Agostinho Neto University, located in the capital of Angola on the Atlantic coast of Africa (−8°50′49.77″; 13°13′51.11″) between June 27th and November 05th, 2023 (Fig. 1). For security reasons, sampling was conducted within the faculty grounds, with the inlet positioned above the guardhouse (~5 m). The sampling site was located in a densely urbanised setting and was subject to mixed traffic- and airport-related influence, being approximately 12 m from a busy avenue and about 400 m from the airport. Luanda, located on the Atlantic coast of Africa, has a humid tropical climate with two main seasons: the cool dry Cacimbo season (June to September) and the rainy season (October to May) (Ministry of Environment of Angola, 2011). Although year-round sampling was not feasible, the campaign was strategically designed to cover the transition between Luanda's two main seasonal regimes, spanning the latter part of the Cacimbo season and the onset of the rainy season. According to 2022 data, the metropolitan area of Luanda is home to over nine million inhabitants – approximately one-third of Angola's total population – making it the country's most densely populated region.

To quantify PM_{10} concentrations, two gravimetric samplers were employed: a high-volume AMS® sampler using 15 cm quartz filters (Pall®) operating at a flow rate of 500 L/min, and a low-volume TECORA® Echo PM unit equipped with 47 mm Teflon filters (Pall®) operating at 38.3 L/min. Quartz filters were pre-baked at 500 °C to eliminate organic residues. All filters were weighed before and after sampling in accordance with the European Standard (EN 12341:2023). Each sampling cycle lasted 23 h 30 min, beginning daily at 06:00 a.m. (local time). After sampling, filters were stored at −18 °C to preserve integrity and weighed under controlled conditions (20 °C, 50% RH) until the standard deviation of at least six measurements was below 2%. Due to occasional power outages, some sampling periods were shorter; only gravimetric data representing more than 75% of a full 24-h cycle were retained. The sampling site was also equipped with a meteorological station and Horiba AP-370 Series gas analysers, which continuously measured NOx, NO, NO_2, CO, and O_3.

Fig. 1. Sampling site location indicated by a red pin (© Google Earth: Accessed Oct. 24th, 2025).

2.2. Particulate matter chemical characterisation

For the analysis of water-soluble anions, cations and anhydrosugars/polyols, half of each Teflon filter was extracted in 8 mL of ultrapure water (Millipore Corporation, USA) using two 15-min sonication cycles. The extracts were filtered through 0.2 μm pore size PVDF membranes (Whatman™, Buckinghamshire, United Kingdom) and divided into three aliquots for subsequent dedicated analysis. The analysed ionic species included SO_4^{2-}, Cl^-, NO_3^-, F^-, NO_2^-, Br^-, PO_4^{3-}, Li^+, Na^+, K^+, NH_4^+, Mg^{2+} and Ca^{2+}. Anhydrosugars and polyols comprised myo-inositol, iso-erythritol, xylitol, arabitol, levoglucosan, ribitol + sorbitol, D-mannitol, mannosan, galactosan, arabinose, galactose, glucose, mannose + xylose, and fructose. The extraction protocols used for inorganic ions and anhydrosugars were based on previously published methods for PM analysis (Domingos et al., 2012; Caseiro et al., 2007; Iinuma et al., 2009), including their subsequent application to PM-bound sugars (Gonçalves et al., 2021). For inorganic ions, validation in PM matrices showed acceptable recoveries in spiked samples (Domingos et al., 2012), whereas the HPAEC-PAD methods adopted for anhydrosugars were based on previously validated protocols for atmospheric aerosol analysis (Caseiro et al., 2007; Iinuma et al., 2009).

Water-soluble inorganic ions were quantified using ion chromatography (Dionex DX-100). For cations, 25 mM H_2SO_4 was used as the eluent and 100 mM tetrabutylammonium hydroxide as the regenerant. For anions, 2.2 mM Na_2CO_3/2.8 mM $NaHCO_3$ served as the eluent, with 50 mM H_2SO_4 as the regenerant. Anhydrosugars and polyols were determined by high-performance anion-exchange chromatography with pulsed amperometric detection (HPAEC-PAD). The mobile phase was programmed with three eluent lines: L1 – ultrapure water, L2 – 200 mM NaOH, and L3 – 5 mM NaOH. Chromatographic separation was performed using a 70-min gradient programme. The run started with 10% L3 for 15 min, followed by a linear increase to 15% L2 over 10 min, reaching 100% L2 at 45 min. The composition was then returned to 10% L3 at 55 min and maintained until the end of the run to allow column re-equilibration (Gonçalves et al., 2021).

The carbonaceous fraction was determined using a thermal–optical protocol inspired by the EUSAAR-II method (European Supersites for Atmospheric Aerosol Research). Samples from quartz filters were heated stepwise in pure N_2 and subsequently in a N_2/O_2 mixture (≈4% O_2) to separate organic carbon (OC) and elemental carbon (EC). Pyrolysed carbon (PC) was quantified and corrected using the laser transmittance signal (LICOR Biosciences, Model LI-6262) once it returned to the initial blank filter value at the first N_2/O_2 step (Pio et al., 2011).

Major and minor elements were quantified after acid digestion of a small section of each quartz filter using a mixture of 1.25 mL HNO_3, 2.5 mL HF, and 1.25 mL $HClO_4$ in 60 mL Savillex vessels on a hot plate. The analyses were performed using two instruments: major elements (Al, Ca, Fe, K, Mg, Mn, Na, P, S, and Ti) were determined by an inductively coupled plasma optical emission spectrometer (ICP-OES, Agilent 5110), while minor elements were quantified by an inductively coupled plasma mass spectrometer (ICP-MS, Agilent 7900). Quality control included analysis of the fly-ash standard reference material NIST-1633c, which was applied to blank filters analysed alongside the samples, using ^{103}Rh as an internal standard. External calibration was carried out with Agilent® multi-element solutions: 0.05–100 ppm for ICP-OES and 1–250 ppb for ICP-MS, both prepared with 5% HNO_3 blanks. Due to the high silicon content of quartz filters, Si was estimated using three times the Al concentrations (Alves et al., 2025). For all analyses, blank samples were measured every ten samples, and their signals were subtracted from the corresponding measurements.

The method detection limits (MDLs) were estimated separately for each analytical platform using method-specific procedures. For water-soluble ions and anhydrosugars/polyols, MDLs were calculated from calibration curve statistics according to Eq. (1), where $se(y)$ is the residual standard error of the regression and *slope* is the slope of the corresponding calibration curve (ICH, 2023). The solution-based values were converted to filter-equivalent values using the extraction volume and the filter-fraction correction factor (Eq. (2)). Finally, air-equivalent values were obtained by dividing the filter-equivalent amount by the sampled air volume (Eq. (3)).

$$MDL_{sol} = \frac{2 \times se(y)}{slope} \tag{1}$$

$$MDL_{filter} = MDL_{sol} \times V_{ext} \times f_{area} \tag{2}$$

$$MDL_{air} = \frac{MDL_{filter}}{V_{sampled}} \tag{3}$$

For elemental analysis by ICP-OES/ICP-MS, MDLs were estimated from the variability of blank filters. The blank standard deviation was used to estimate the MDL for the digested filter portion (Eq. (4)), which was then scaled to the full sampled filter area (Eq. (5)) and expressed on an air-volume basis (Eq. (6)), following blank-based detection-limit approaches used in ambient particulate-matter ICP analysis (U.S. EPA, 2017).

$$MDL_{portion} = 3.33 \times SD_{corrected\ blank} \tag{4}$$

$$MDL_{filter} = MDL_{portion} \times \frac{A_{total}}{A_{digested}} \tag{5}$$

$$MDL_{air} = \frac{MDL_{filter}}{V_{sampled}} \tag{6}$$

For TC, OC and EC, minimum relative uncertainties of 5%, 5% and 10%, respectively, were adopted for PMF input. These values were selected as pragmatic lower-bound estimates consistent with reproducibility reported for thermal–optical carbon analysis, for which uncertainties are generally lower for TC and OC than for EC (Sipkens et al., 2024; Cavalli et al., 2010).

Chloride depletion was estimated from the deviation of the molar Cl^-/Na^+ ratio in the marine factor from the reference seawater ratio of 1.16, following approaches commonly used to assess sea-salt ageing (Su et al., 2022; Zhou et al., 2025). For this calculation, Cl^- and Na^+ mass concentrations assigned to the factor were first converted to molar concentrations. Sea salt sulphate was estimated from the Na^+ mass concentration assigned to the factor using the seawater SO_4^{2-}/Na^+ mass ratio of 0.252, and non-sea-salt sulphate was calculated by subtracting the estimated sea salt sulphate from the total sulphate assigned to the same factor (Sciare et al., 2005). These calculations were used to evaluate chloride depletion and the contribution of non-sea-salt sulphate within the marine aerosol factor.

$$Cl^- \text{ depletion}(\%) = \left[1 - \frac{(Cl^-/Na^+)}{1.16}\right] \times 100 \tag{7}$$

$$\text{ss-}SO_4^{2-} = Na^+ \times 0.252 \tag{8}$$

$$\text{nss-}SO_4^{2-} = SO_4^{2-} - \text{ss-}SO_4^{2-} \tag{9}$$

2.3. Source apportionment by Positive Matrix Factorisation

Source apportionment was conducted using the United States Environmental Protection Agency (U.S. EPA) Positive Matrix Factorisation (PMF) model Version 5.0.14 (Norris et al., 2014). The input matrix consisted of measured concentrations and another one with their corresponding uncertainties. Following data-quality recommendations for PMF input, concentrations below the MDL and their associated uncertainties were treated according to equations (10) and (11), as recommended in the EPA manual (Norris et al., 2014):

$$C_{ij} = \begin{cases} \frac{MDL_{ij}}{2}, C_{ij} \leq MDL \\ C_{ij}, C_{ij} > MDL \end{cases} \quad (10)$$

$$Unc_{ij} = \begin{cases} (5/6) \times MDL_{ij}, C_{ij} \leq MDL \\ \sqrt{(0.05 \times C_{ij})^2 + (0.5 \times MDL_j)^2}, C_{ij} > MDL \end{cases} \quad (11)$$

where *"Unc"* is the uncertainty, *"MDL"* is the method detection limit, and *"C"* is the concentration of species *"j"* in sample *"i"*. For missing samples, the uncertainty was set to four times the species median, reducing its weight in the model.

To estimate the optimal number of factors, equation (12) was used, where $Q_{(Expected)}$ was calculated using equation (13) based on the number of samples (m), species (n) and factors (f) (Brown et al., 2015; Pereira et al., 2017). The number of factors was progressively increased until further reductions in the $Q_{(Robust)}/Q_{(Expected)}$ ratio became insignificant, as illustrated in Fig. S1.

$$Q_{(Robust)} / Q_{(Expected)} \quad (12)$$

$$Q_{(Expected)} = m^*n - f\,(m+n) \quad (13)$$

In total, 129 daily samples and 27 chemical species were included in the PMF input matrix. Species were initially categorised following the EPA PMF 5.0 framework, using signal-to-noise ratio (S/N) together with broader data-quality considerations. As in previous PMF applications, species with S/N > 2 were treated as strong, those with 0.2 ≤ S/N ≤ 2 as weak, and those with S/N < 0.2 as bad, with weak species down-weighted and bad species excluded from the analysis (Kebe et al., 2021; Norris et al., 2014). In the present study, this initial classification was further refined through iterative PMF testing, taking into account observed–predicted fit for individual species, scaled residuals, temporal consistency, and tracer relevance for source identification (Fakhri et al., 2024; Huang et al., 2018; Liu et al., 2025). Accordingly, species with similar S/N values were not necessarily assigned to the same final category. In the final input matrix, 11 species were classified as strong and 16 as weak (Table 1). Concentration statistics, MDLs, missing values and below-detection-limit counts for the full set of analysed species are provided in the Supplementary Material. For the additional saccharide and polyol tracers not retained in the PMF input matrix, the high proportion of values below detection and their weak temporal robustness limited their usefulness for source apportionment; consequently, levoglucosan was the only sugar-derived tracer retained in the final PMF input.

The optimal solution was determined based on the stability of the $Q_{(Robust)}/Q_{(Expected)}$ ratio, residual distribution, factor interpretability, and the outcomes of the Displacement (DISP) and Bootstrap (BS) diagnostics (Kebe et al., 2021; Cipoli et al., 2023). The analysis was conducted without constraining any factors, in order to avoid artificial bias and preserve a fully data-driven solution. The "extra modelling uncertainty" parameter was set to 5%.

2.4. Supporting analyses and data processing

Meteorological data from the local station were used to investigate short-range aerosol transport through directional analyses in the openair R package, including polarPlot and the Conditional Probability Function (CPF), based on the daily fractional contributions of the PMF factors (Carslaw and Ropkins, 2012; Hopke, 2010). Regional transport was assessed using 120 h backward air-mass trajectories calculated every 24 h with HYSPLIT (v5.3.0), driven by the NCEP/NCAR reanalysis dataset (2.5° spatial resolution) at 500 m above ground level (Rolph et al., 2017; Stein et al., 2015). Back-trajectory clustering was performed for the full sampling campaign (27 June–5 November 2023) using all daily trajectories. These analyses supported the interpretation of PMF factors and the identification of potential source regions. Additional meteorological and trajectory clustering details are provided in the Supplementary Material (Figs. S2 and S3).

Active-fire activity was qualitatively assessed using MODIS Collection 6.1 and VIIRS NOAA-20 (JPSS-1) products from NASA FIRMS (NASA MODIS Science Data Support Team, 2021; NASA VIIRS Land Science Team, 2020). Hotspot detections and 375 m fire data were extracted for southern Africa, and selected KML/KMZ layers were visualised in Google Earth Pro to produce fire maps of detection density and distribution.

Table 1
Statistics for the constituents that served as input for the PMF.

Species	Unit	Min ± Unc	Median ± Unc	Max ± Unc	Ave ± STD	Cat	S/N	R^2 (vs PM_{10})
PM_{10}	μg/m^3	23.6 ± 0.471	56.3 ± 1.13	108 ± 2.15	59.4 ± 15.6	Weak	10	1
Cl^-	μg/m^3	0.344 ± 0.0245	1.25 ± 0.0655	5.76 ± 0.289	1.57 ± 1.14	Weak	9	0.02
NO_3^-	μg/m^3	0.776 ± 0.0574	2.09 ± 0.113	7.1 ± 0.357	2.50 ± 1.37	Strong	9	0.82
NH_4^+	μg/m^3	0.00668 ± 0.011	0.157 ± 0.0658	1.32 ± 0.0773	0.303 ± 0.313	Weak	3.6	0.33
SO_4^{2-}	μg/m^3	0.553 ± 0.922	2.18 ± 0.13	7.12 ± 0.362	2.65 ± 1.23	Strong	10	0.59
EC	μg/m^3	1.92 ± 0.0962	8.76 ± 0.438	22.1 ± 1.11	9.41 ± 3.62	Strong	10	0.47
OC	μg/m^3	4.01 ± 0.2	8.85 ± 0.442	19.4 ± 0.968	9.83 ± 3.76	Strong	10	0.75
Li	ng/m^3	0.152 ± 0.0331	0.448 ± 0.0392	1.42 ± 0.0781	0.494 ± 0.211	Strong	9.2	0.53
V	ng/m^3	0.854 ± 0.0432	2.09 ± 0.105	5.32 ± 0.266	2.24 ± 0.803	Strong	10	0.71
Cr	ng/m^3	0.573 ± 0.954	3.45 ± 0.598	9.26 ± 0.736	3.41 ± 1.31	Weak	4.6	0.35
Ni	ng/m^3	<0.317 ± 0.529	3.85 ± 0.371	13.6 ± 0.749	4.73 ± 3.90	Weak	6.9	0.17
Cu	ng/m^3	3.10 ± 0.872	8.97 ± 0.966	30.8 ± 1.76	10.2 ± 4.67	Weak	8	0.27
Zn	ng/m^3	14.9 ± 24.9	82.5 ± 15.5	863 ± 45.7	153 ± 163	Weak	5.1	0.08
Cd	ng/m^3	0.105 ± 0.0191	0.395 ± 0.027	3.33 ± 0.167	0.557 ± 0.531	Weak	10	0.20
Sn	ng/m^3	0.399 ± 0.0502	1.46 ± 0.0864	5.26 ± 0.267	1.72 ± 0.837	Weak	10	0.33
Sb	ng/m^3	1.22 ± 0.0793	3.40 ± 0.178	7.64 ± 0.385	3.65 ± 1.25	Weak	10	0.38
Ba	ng/m^3	8.00 ± 0.605	36.0 ± 1.86	101 ± 5.08	43.0 ± 20.3	Weak	10	0.36
Pb	ng/m^3	1.82 ± 0.143	8.00 ± 0.415	126 ± 6.30	17.8 ± 22.1	Weak	10	0.14
Al	μg/m^3	0.398 ± 0.0447	1.28 ± 0.0753	3.01 ± 0.156	1.35 ± 0.542	Strong	10	0.67
Ca	μg/m^3	0.832 ± 0.0841	2.46 ± 0.143	4.2 ± 0.222	2.56 ± 0.674	Strong	10	0.60
Fe	μg/m^3	0.326 ± 0.017	1.1 ± 0.0554	2.54 ± 0.127	1.14 ± 0.357	Strong	10	0.72
K	μg/m^3	0.0738 ± 0.0333	0.535 ± 0.0426	2.21 ± 0.115	0.688 ± 0.493	Strong	8.3	0.74
Mg	μg/m^3	0.194 ± 0.0164	0.411 ± 0.0244	1.32 ± 0.0673	0.453 ± 0.18	Weak	10	0.33
Na	μg/m^3	0.422 ± 0.068	1.26 ± 0.0903	2.51 ± 0.142	1.35 ± 0.53	Weak	7.9	0.02
P	μg/m^3	0.0133 ± 0.0222	0.0584 ± 0.0136	0.135 ± 0.0149	0.0614 ± 0.0256	Weak	3	0.71
Ti	μg/m^3	0.0267 ± 0.0013	0.0725 ± 0.0036	0.191 ± 0.00954	0.0781 ± 0.028	Strong	10	0.63
Si	μg/m^3	1.19 ± 0.134	3.83 ± 0.226	9.03 ± 0.469	4.06 ± 1.62	Strong	10	0.67
Levo	μg/m^3	0.0131 ± 0.0218	0.109 ± 0.0192	0.482 ± 0.0276	0.122 ± 0.0801	Weak	4.1	0.45

Statistical analyses were performed in Python using pandas, NumPy, statsmodels, and scipy. stats. Descriptive statistics, linear regressions, Spearman correlations, and graphical outputs, including temporal trends, weekly boxplots and distributional patterns, were produced using Matplotlib and seaborn.

3. Results and discussion

3.1. Overview of meteorological conditions

Luanda's meteorology during the campaign was marked by moderate solar radiation (134 ± 45 W m^{-2}), mild temperatures (23.7 ± 2.41 °C), persistently high relative humidity (80.7 ± 8.33%), low pressure variability (1008 ± 2.37 mbar), and moderate winds (1.51 ± 0.47 m s^{-1}), with afternoon peaks from the southwest between 14:00 and 17:00 (Fig. S4). The sampling period covered late Cacimbo – a cool, dry season with morning fog and typical temperatures of 22–25 °C – and the warmer transition to the rainy season, when temperatures may reach ~30 °C. In line with Luanda's climate, controlled by the South Atlantic anticyclone and modulated by sea breezes and local surface characteristics (Huntley et al., 2019), seasonal contrasts were mainly driven by temperature and rainfall (Table S1). Compared with late Cacimbo, the rainy season onset was warmer (26.0 vs 22.9 °C), slightly windier (1.61 vs 1.46 m s^{-1}), and somewhat sunnier (146 vs 130 W m^{-2}), whereas relative humidity remained similar (~81%). Rainfall showed the sharpest transition: despite mostly dry conditions, intense events (>6 mm h^{-1}) occurred on 24 October and 1 November 2023, indicating the progressive establishment of wetter October-November conditions.

For atmospheric context of the PMF-resolved sources, Fig. S5 summarises the temporal behaviour of the gaseous pollutants measured continuously at the same site and during the same campaign as the PM_{10} sampling (da Silva et al., 2025). CO remained relatively stable, although higher concentrations were observed during the earlier part of the campaign, with a mean value of 0.90 ± 0.76 ppm. NO and NO_2 showed marked day-to-day variability, averaging 33.9 ± 40.8 and 17.7 ± 14.2 ppb, respectively, and NO_2 frequently exceeded the WHO 24 h guideline. O_3 remained comparatively low (14.0 ± 7.6 ppb) and decreased slightly from August to September (Table S2). Together, these patterns are consistent with a traffic-influenced urban atmosphere and with surface ozone variability that was shaped more by mixing and NO_x-related processes than by sustained local photochemical build-up. PM_{10} remained persistently elevated throughout the campaign, with daily concentrations averaging 59.3 μg m^{-3} and exceeding the WHO 24 h guideline on most sampled days. Concentrations were generally higher and more variable during the earlier, drier part of the campaign, whereas lower values became more frequent towards the later sampling period, consistent with the transition from the Cacimbo season to the onset of the rainy season (da Silva et al., 2025). The selected PM_{10} species covered the main aerosol components and source tracers, including carbonaceous material, secondary inorganic ions, marine markers, crustal elements, and traffic-/industry-related trace metals (Table 1).

3.2. Source apportionment

Among the tested solutions, the reduction in $Q_{(Robust)}/Q_{(Expected)}$ was substantial from six to seven factors but negligible beyond seven, suggesting that the optimal number of factors lies near this range (Fig. S1). The six-factor solution was therefore retained as a stable and interpretable configuration, with a consistent residual distribution and robust performance in both Displacement (DISP) and Bootstrap (BS) diagnostics (Table S3–S5). Accordingly, six factors were identified: Factor 1, associated with non-ferrous metallurgy and the handling and burning of galvanised or metal scrap; Factor 2, representing traffic emissions from both exhaust and non-exhaust processes; Factor 3, related to crustal material and resuspended dust; Factor 4, linked to a metallurgical nickel source with an aviation overlay; Factor 5, associated with marine aerosol; and Factor 6, corresponding to secondary aerosol (SA) combined with biomass burning (BB). The relative source contributions and their temporal evolution are summarised in Fig. 2.

Bootstrap mapping (Table S3) shows that Factor 1 (Metallurgy & scrap), Factor 2 (Traffic emissions) and Factor 4 (Ni source with an aviation overlay) are fully stable, showing 100% consistency. Factor 5 (Marine aerosol) and Factor 6 (SA + BB) also display high stability, with 99% consistency and only 1% reallocated to Factor 2. The only meaningful cross-mapping occurs for Factor 3 (Crustal/resuspended dust), which shows 81% consistency, while 19% of the runs are reallocated to Factor 2. No factor appears in the "Unmapped" category. DISP diagnostics further show that factor identities are largely maintained under rotational stress (Table S4). At the lowest dQ perturbation levels, no swaps occur, and even at the highest perturbation only Factors 2, 3 and 6 exhibit swaps, with a maximum of 9. All tested F_{peak} (Table S5) values (−1.0 to +1.5) increased $Q_{(robust)}$ relative to the base run ($F_{peak} = 0$), with changes ranging from about 5% to over 50%. None of the rotated solutions yielded a lower $Q_{(robust)}$, nor did they improve the interpretability of profiles or contributions. The $F_{peak} = 0$ solution was therefore retained as the final model, which reproduced PM_{10} mass with excellent agreement, yielding $R^2 = 0.95$ and RMSE = 3.95 μg m^{-3} between reconstructed and measured concentrations (Fig. S6). The chemical profiles of each factor are depicted in Fig. 3.

A mass reconstruction was performed by grouping the measured species into major aerosol components. On average, PM_{10} was composed of 27.4% ± 5.38% organic matter, 16.1% ± 4.40% elemental carbon, 33.9% ± 5.60% major element oxides, 13.3% ± 3.3% water-soluble ions, 0.9% ± 0.9% anhydrosugars/polyols, and 4.6% ± 1.5% particle-bound water (estimated based on Köhler theory), leaving a residual unexplained fraction of 5.3% ± 8.4%. This limited residual indicates that the measured chemical species captured the dominant PM_{10} components, with no major unmeasured fraction evident prior to source apportionment.

3.2.1. Factor 1: non-ferrous metallurgy + galvanised/metal scrap handling and burning

Different anthropogenic activities exhibit characteristic chemical fingerprints involving Pb, Zn, Cd, Sn and Sb, producing profiles that are clearly distinguishable from natural crustal material (Fig. 3). Although Zn and Cd may occur together in mineral matrices due to their co-occurrence in sulphide minerals (National Research Council, 1974; Ramírez et al., 2020) previous work in Luanda has demonstrated a predominantly anthropogenic origin for these elements in PM_{10} (Alves et al., 2025). The factor resolved in this study exhibits substantial contributions of Zn (76.2%), Pb (79.6%), Sb (20.2%) and Sn (38.6%), yielding Zn/Pb = 8.51, Zn/Cd = 362, Zn/Sn = 170 and Zn/Sb = 159. These ratios point to a Zn-dominated chemical profile that is incompatible with emissions from lead–acid battery recycling, which typically produce extremely low Zn/Pb and Zn/Cd ratios (e.g., Zn/Pb = 0.01–0.13; Zn/Cd = 0.07–2.2) (Kelektsoglou et al., 2018). Instead, the concurrent presence of Zn, Pb, Cd and Sn in elevated proportions is a recognised signature of non-ferrous metallurgical activities, high-temperature galvanising or electroplating operations, and informal electronic-waste processing (Bozkurt et al., 2018; Kara et al., 2015; Ogundele et al., 2016; Soni et al., 2019). In such settings, Pb and Cd frequently appear as minor co-contaminants because Pb may be added to Zn coatings for mechanical properties, and both Pb and Cd can volatilise during high-temperature galvanising (Begum and Hopke, 2019; National Research Council, 1974; Pabroa et al., 2022). Emission guidelines and environmental assessments for galvanising facilities document the same patterns (ADEM, 2025; DSEWPaC, 2012).

Comparison with SPECIEUROPE profiles further supports this interpretation. Profile 229 (zinc galvanising) is dominated by refined Zn and contains negligible Pb and Cd, whereas the profile resolved here more closely resembles Profile 79, representing scrap-metal

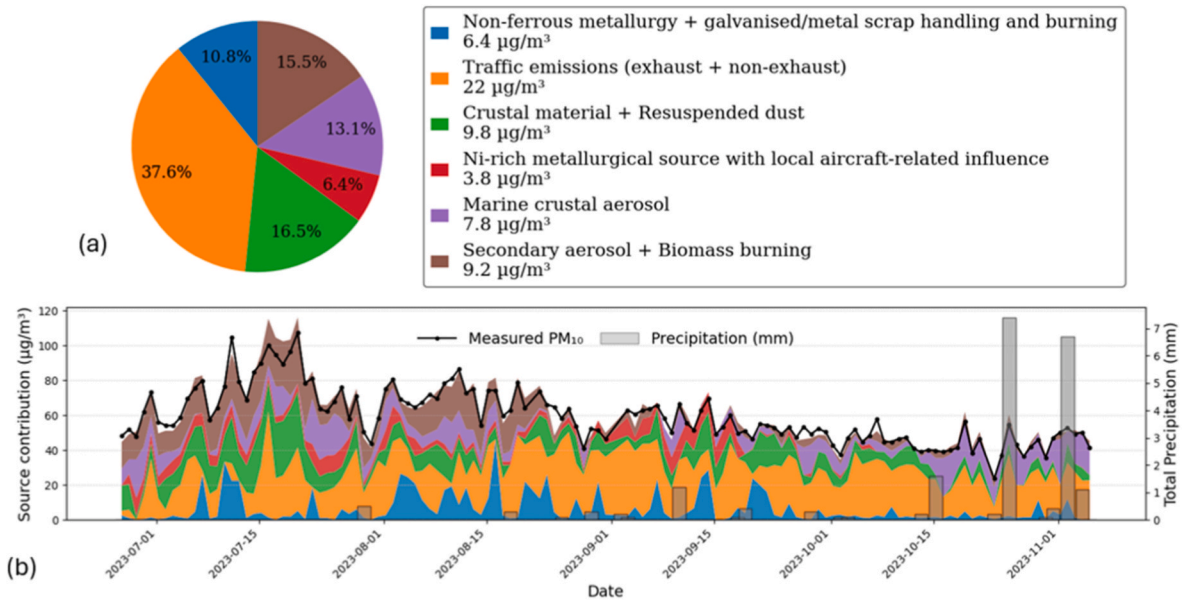

Fig. 2. Source apportionment by PMF: (a) overview of the relative mean contribution of each source; (b) time series of daily source contributions over the campaign period, overlaid with measured PM_{10} and precipitation (mm).

incineration, characterised by similarly elevated Zn/Pb and Zn/Cd ratios (Pernigotti et al., 2016). Additional evidence from studies in regions dominated by non-ferrous metallurgy shows Zn-rich ambient signatures where Zn greatly exceeds Pb, Cd and Sn, consistent with emissions from alloyed and galvanised scrap materials (Hsu et al., 2021; Lee et al., 2023). Ratios can vary with distance from the source, but remain within comparable ranges - for example, near a scrap iron and steel smelting facility in Nigeria, $PM_{2.5}$ exhibited Zn/Pb = 9.7, Zn/Cd = 290 and Zn/Sn = 123, reflecting co-contaminants emitted during metallurgical processes, e-waste burning and galvanised steel handling (Owoade et al., 2015).

The directional behaviour of this factor is complex, but an overall easterly influence emerges from the polar plot and the higher mean HYSPLIT cluster concentrations associated with air masses arriving from the east (Table 2, Figs. 4a and 5). This aligns with the location of the Luanda landfill, where informal scrap recovery, including open burning of galvanised materials and electronic waste, is well documented. The temporal pattern - episodic peaks mostly early in the week, followed by declining concentrations - supports the hypothesis of periodic burning linked to waste-handling routines. The highest daily concentrations were recorded on 16 August (46.2 µg m^{-3}), 10 July (33.3 µg m^{-3}) and 14 September (28.7 µg m^{-3}).

Overall, the chemical profile, elemental ratios, and directional/temporal characteristics consistently indicate that this PMF factor represents emissions from mixed non-ferrous metallurgical activities combined with informal scrap-metal and e-waste processing, likely concentrated in the eastern sector of Luanda. It accounts for approximately 10.8% of the total PM_{10} mass and reflects a recognised local emission scenario.

3.2.2. *Factor 2: traffic emissions (exhaust + non-exhaust)*

This factor represents the largest contribution to PM_{10}, accounting for 37.6% of the mass. The chemical profile combines markers of exhaust emissions (EC, OC), abrasive non-exhaust wear (Fe, Ba, Cu, Sb, Sn, Zn), and road dust resuspension (Ca, Al, K, Mg, Ti). Such mixtures are expected in urban settings where PMF struggles to isolate traffic components into distinct factors because of shared tracer species and physical interactions between vehicles and the road surface (Almeida et al., 2022; Demir et al., 2022; Querol et al., 2013).

Elemental ratios further characterise the mixed nature of this factor: Cu/Sb = 2.62 and Zn/Sb = 9.97, which are typical of brake wear, while a high Fe/Cu ratio (81.7) indicates a substantial resuspended soil contribution (Alves et al., 2025). Local conditions favour this mixture, as large portions of Luanda's peri-urban and informal areas remain unpaved, supplying mineral particles available for vehicular resuspension (Benmaamar et al., 2020). Nevertheless, the dominant presence of EC (58.4%) clearly indicates a strong contribution from primary vehicular combustion. The OC/EC ratio of 0.69 is also consistent with traffic emissions influenced by diesel combustion (Alves et al., 2020; Ancelet et al., 2011; Brito et al., 2013; Charron et al., 2019). Given regional fleet characteristics, contributions from older, pre-DPF diesel vehicles are plausible (Alves et al., 2015; Geller et al., 2006). The BS-DISP results confirmed some rotational ambiguity, reflecting the overlapping chemical signatures. However, this uncertainty is consistent with the mixed traffic nature of the factor rather than with a purely non-exhaust profile.

Meteorological analysis (Fig. 4b and Table 2) shows moderate modulation by regional transport. HYSPLIT trajectories indicate higher concentrations under southern flows and lower levels under easterly trajectories, while polar plots reveal an additional westerly influence, suggesting a combined local–regional transport regime with maximum contributions from the south-east sector. No marked seasonal trend was detected. Peak values were observed on 16 July (60.9 µg m^{-3}), 19 August (49.4 µg m^{-3}) and 26 August (47.3 µg m^{-3}). Weekly patterns were generally stable, as expected for continuous urban traffic, with occasional elevated values toward the end of the week.

3.2.3. *Factor 3: crustal material + resuspended dust*

This factor is characterised by high contributions of Al, Si, Ca, Fe, Ti, Mg, K and Li, along with moderate Na and P, indicating a dominant crustal material and resuspended dust source (Alghamdi et al., 2015; Cipoli et al., 2023; Liu et al., 2022). The PMF isolated a dust factor contributing 16.5% of PM_{10}, although the oxide-conversion method applied to the same dataset yielded a higher estimate (31 ± 5%) (Alves et al., 2025). This difference suggests that mineral matter was not over-allocated to a single PMF factor and was likely partly redistributed into other factors, especially traffic, owing to shared tracers and the physical coupling between road dust and vehicular resuspension. This interpretation is further supported by a companion elemental study based on the same sampling campaign, in which crustal enrichment

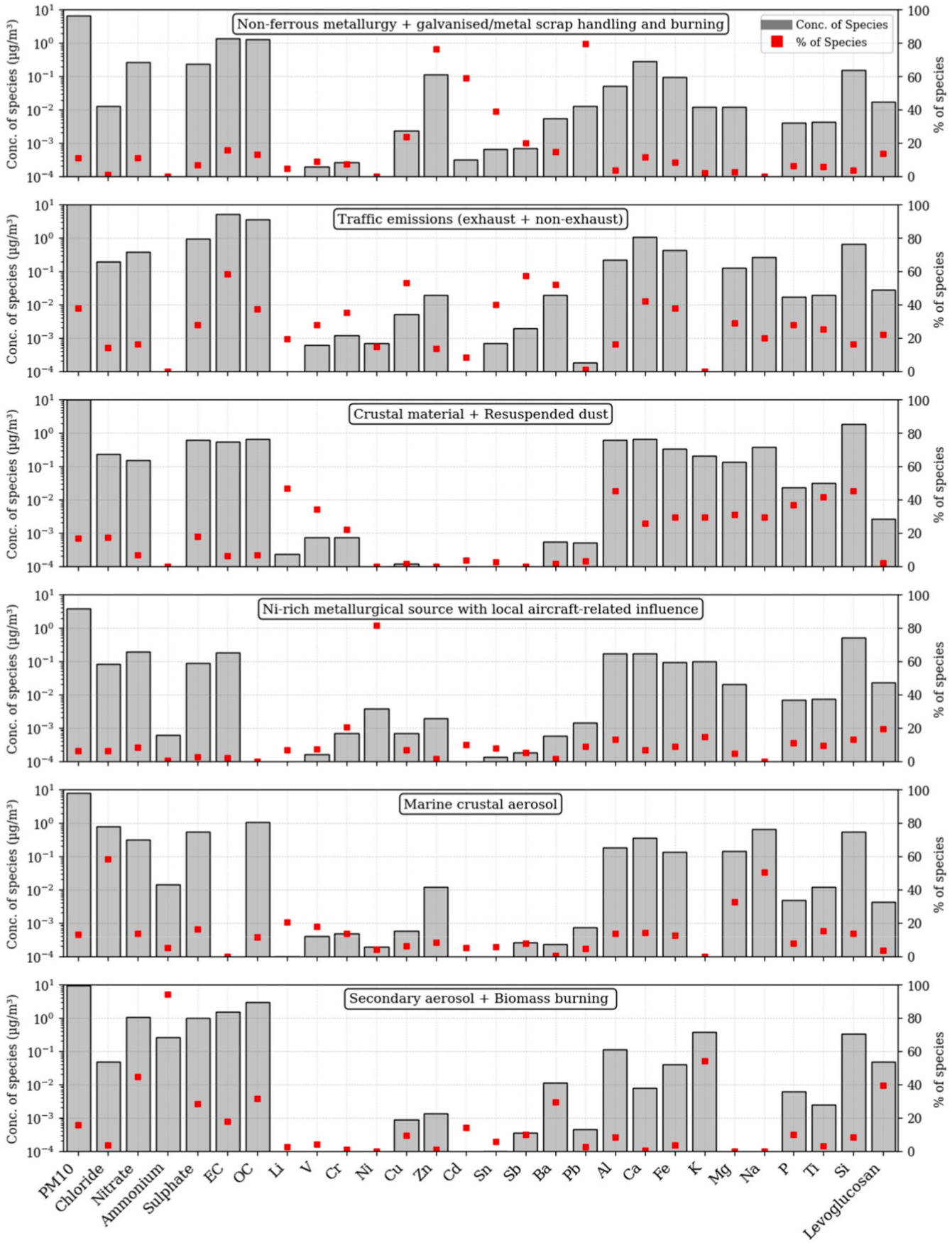

Fig. 3. Chemical profiles of the six factors resolved by the PMF 5.0 model for Luanda, showing species concentrations (bars) and percentage contributions (% of species, red squares).

Table 2
Mean concentrations of the six PMF-resolved factors and ozone under different air mass clusters (CLT 1–4) identified by HYSPLIT.

CLT	Factor 1 (μg m^{-3})	Factor 2 (μg m^{-3})	Factor 3 (μg m^{-3})	Factor 4 (μg m^{-3})	Factor 5 (μg m^{-3})	Factor 6 (μg m^{-3})	O_3 (ppb)
1	7.8	20.1	14.8	4.7	9.0	18.0	16.3
2	7.1	23.4	9.1	4.8	12.0	7.9	13.2
3	4.9	26.4	8.3	5.3	7.1	5.9	12.4
4	10.6	17.9	13.6	5.1	8.7	15.7	18.2

factors (CEF) and geoaccumulation indices (Igeo) indicated largely geogenic behaviour for lithophile elements such as Fe, Ca and Al, whereas strongly enriched metals such as Sb, Cd, Zn, Pb, Cu and Sn were associated with non-crustal inputs (Alves et al., 2025). The chemical composition provides additional support for this interpretation: the high Cu/Sb ratio (47.6) and the negligible contribution of Zn suggest limited mixing with the metal-enriched anthropogenic factors, while the major mineral tracers remained concentrated in this profile. Overall, this factor is best interpreted as predominantly crustal/resuspended mineral dust rather than as a chemically pristine soil profile.

The temporal and meteorological patterns align with soil and dust resuspension driven primarily by meteorology rather than anthropogenic cycles (Figs. 4c and 5). No marked seasonal pattern emerged, but higher concentrations occurred during the dry season inland-flow periods, especially between 11 and 20 July, when HYSPLIT clusters CLT 1 and CLT 4 transported air masses across inland Angola (Table 2). Polar plots show this factor is almost exclusively associated with southeasterly winds, and the CPF indicates highest contributions under low relative humidity and high solar radiation, conditions that favour particle resuspension. Weekly behaviour was relatively uniform on working days (10.6 ± 0.73 μg m^{-3}) with slightly lower values on weekends (7.99 ± 0.08 μg m^{-3}). This subtle weekday/weekend contrast suggests a small additional contribution from human activity, but the factor remains predominantly controlled by meteorological drivers (Fig. 6c).

3.2.4. *Factor 4: Ni-rich metallurgical source with local aircraft-related influence*

Factor 4 is characterised by a strong enrichment in Ni, which accounts for most of the Ni measured during the campaign while contributing only a small fraction of the total PM_{10} mass (≈6.4%). Its chemical signature is marked by a high Fe/Ni ratio (~25), extremely low V (V/Ni ≈ 0.04), and only moderate sulphate, with minor but consistent amounts of Zn, Pb and Cu. This pattern is not consistent with a typical heavy-fuel-oil or shipping-related profile, which generally shows markedly higher V/Ni ratios together with a clearer association between Ni, V and sulphate (Viana et al., 2009; Becagli et al., 2012). Instead, the profile is more consistent with a local Ni-rich source of industrial or mechanical character, possibly related to the handling, abrasion, processing, or resuspension of Ni-bearing materials. In this context, the concomitant presence of Fe and Cr is more consistent with a local metal-rich source than with residual-oil combustion. Previous studies indicate that atmospheric Ni may arise from strongly localised industrial sources and that Ni-rich ambient concentrations are not necessarily linked to shipping or heavy-oil combustion (Okuda et al., 2007; Font et al., 2022).

The secondary occurrence of Cu and Zn suggests mechanical wear that could include an airport-related overlay, although not with an exclusive aviation attribution (Amato et al., 2010). More broadly, airport environments can generate particulate metals through tyre wear, brake wear, runway abrasion, resuspension, and engine-related processes, but most of these tracers are not unique to aviation and overlap with other urban non-exhaust sources (Masiol and Harrison, 2014; Masiol et al., 2017; Massas et al., 2018). Pb is not, on its own, a specific tracer of airport activity, and Ni in airport environments should not be interpreted solely as a product of fuel combustion. Fresh aircraft exhaust particles may contain Ni, Cu, Pb and Zn, but these metals can derive from overlapping contributions, including trace fuel or lubrication-oil impurities and engine wear, and are therefore not diagnostic when considered in isolation (Abegglen et al., 2016; Turgut et al., 2019). Moreover, lead emissions in airport environments are primarily associated with piston-engine aircraft using leaded avgas rather than with commercial jet operations (U.S. EPA, 2020; U.S. EPA, 2023). Overall, the available evidence supports, at most, a possible airport-related superposition on a dominant local Ni-rich source rather than a distinct aviation factor.

The temporal pattern (Figs. 4d and 5) is also consistent with this interpretation. The factor exhibits a relatively stable background without strong seasonal variability, suggestive of a continuous local anthropogenic emission, and remains present over several weeks, with sustained contributions from July to mid-September followed by a sharp decline after approximately 20/09/2023. This behaviour is more consistent with a recurring local source regime than with a single isolated event. At the same time, the marked regime change may have increased the statistical separation of Ni in the PMF solution, and this possibility should be acknowledged explicitly, since receptor models resolve factors from covariance structure and may be influenced by temporally strong episodes (Norris et al., 2014; Brown et al., 2015). Its higher contributions under low wind-speed conditions, together with the absence of evidence for long-range transport in the trajectory analysis, are more consistent with a nearby source, possibly influenced by sectors that also include airport-related activities, than with regional transport or shipping emissions.

3.2.5. *Factor 5: marine-crustal aerosol*

The clear contribution of sodium (50.4%), chloride (58.3%) and magnesium (32.6%) strongly supports the identification of this factor as a sea-salt-dominated marine–crustal aerosol source (Alfeus et al., 2024; Cipoli et al., 2023). It accounted for ~13.1% of PM_{10}, consistent with expected sea-salt influence at a coastal urban site. The sampling location, situated approximately 4 km inland, lies within the zone affected by sea–land breeze circulations. Such pressure-driven convection readily transports sea-salt aerosol inland (Lu and Turco, 1994). Despite its clear chemical signature, the meteorological diagnostics indicate a relatively diffuse transport pattern (Figs. 4e and 5). Neither the HYSPLIT back-trajectories nor the polar plot show a single dominant directional sector. However, when analysed together with temperature and solar radiation, enhanced contributions under southerly to south-easterly flow may reflect the influence of local coastal circulation and mixed marine–urban air masses, rather than a single well-defined transport corridor. The factor molar Cl^-/Na^+ ratio (0.79) was below the seawater reference value (1.16), indicating 32% chloride depletion and therefore some atmospheric ageing (Su et al., 2022; Zhou et al., 2025). This is consistent with studies showing that fresh sea salt typically has Na–Cl–Mg-rich profiles close to seawater composition, whereas aged sea salt exhibits chloride loss and increasing association with nitrate and/or sulphate (Corral et al., 2020; Fomba et al., 2014). However, non-sea-salt sulphate remained low (0.39 μg m^{-3}; ~6.5% of the sulphate assigned to the factor), suggesting only moderate secondary processing.

3.2.6. *Factor 6: secondary aerosol + biomass burning*

Factor 6 exhibits a characteristic chemical signature dominated by SA components mixed with BB tracers, accounting for 15.5% of PM_{10} mass (Bao et al., 2023; Cipoli et al., 2023; Srivastava et al., 2021). The factor is characterised by ammonium (94.4% of total NH_4^+) accompanied by substantial contributions from nitrate (44.5% of total NO_3^-) and sulphate (28.4% of total SO_4^{2-}). In addition, clear BB markers were identified, notably levoglucosan (39.6% of $C_6H_{10}O_5$), a specific molecular BB tracer, and the complementary inorganic tracer K (54.1% of K), which is not source-specific since it also originates from mineral dust, sea salt, and other sources (Tao et al., 2016; Zhang et al., 2010). In many PMF applications, SA and BB tracers are resolved as distinct profiles: one

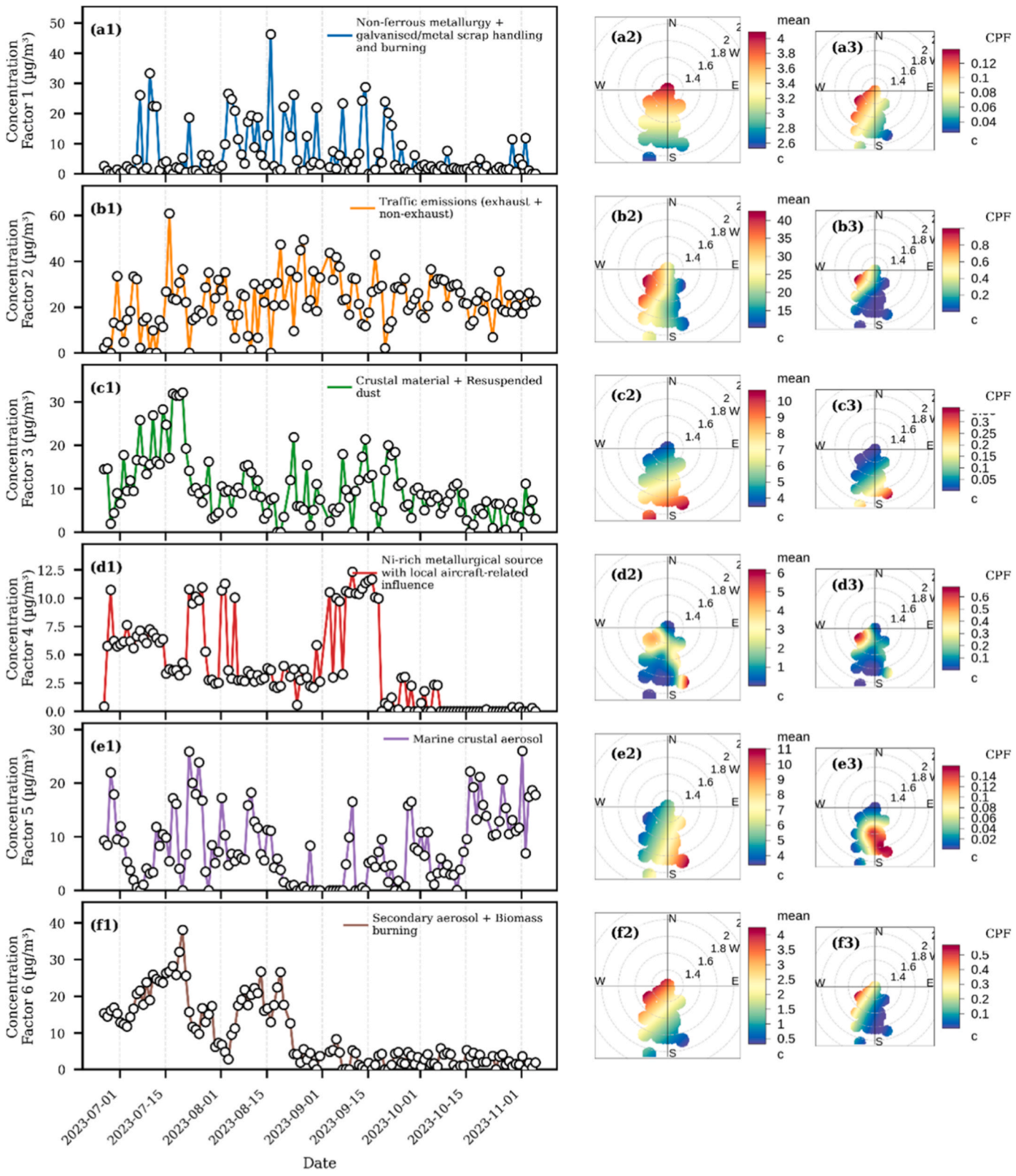

Fig. 4. Temporal evolution, bivariate polar plots of mean concentration, and conditional probability function (CPF) plots for the six PMF-resolved factors at the Luanda sampling site during the PM_{10} campaign. Each row corresponds to one factor. Left-hand panels show the factor concentration time series, middle panels show bivariate polar plots of mean factor concentration as a function of wind direction and wind speed, and right-hand panels show the corresponding CPF plots calculated at the 75th percentile.

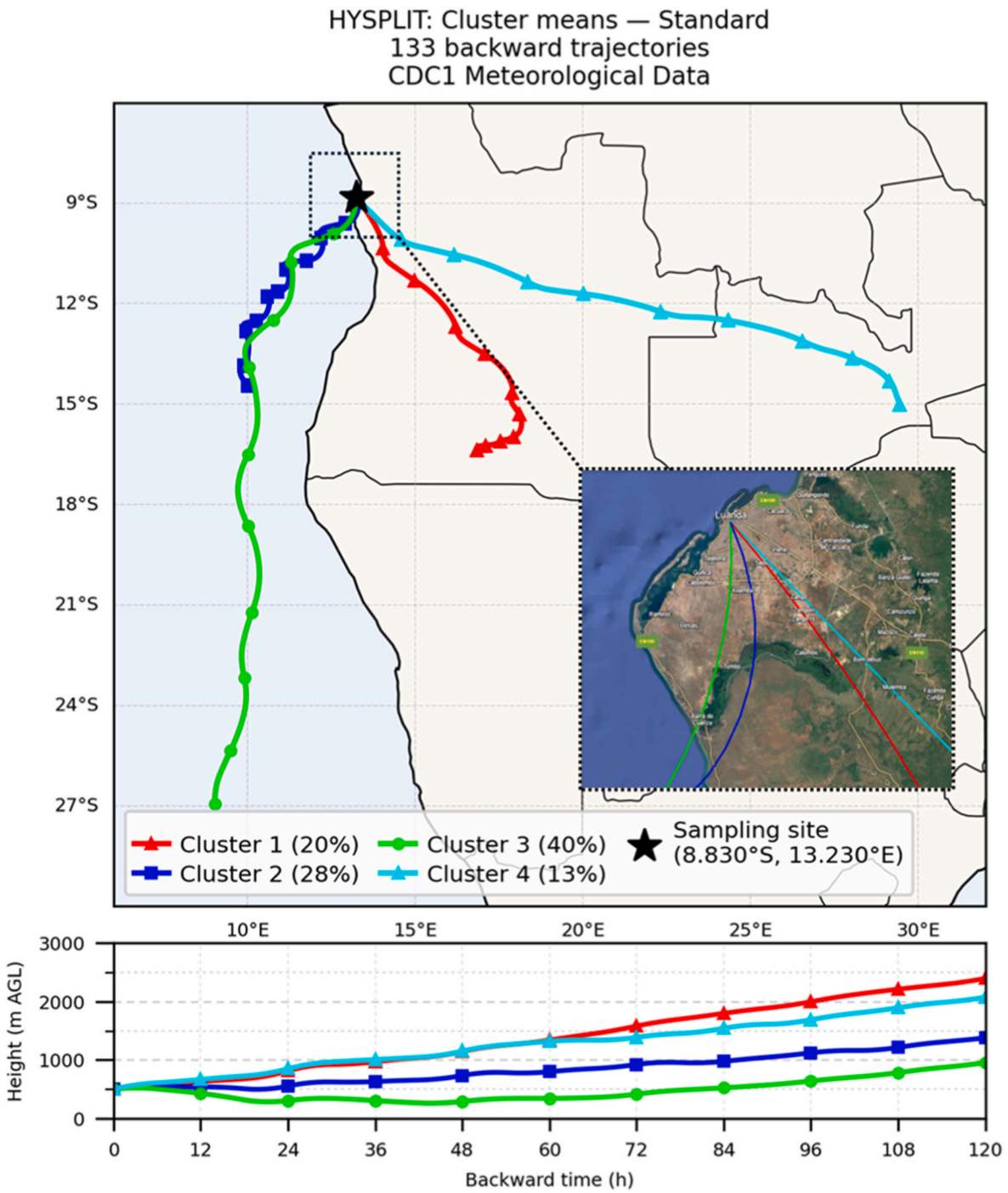

Fig. 5. Cluster-mean backward trajectories using HYSPLIT. The four main air mass clusters are: Cluster 1 (red, 20%) from the southwestern continental sector, Cluster 2 (blue, 28%) and Cluster 3 (green, 40%) from the southern Atlantic marine sector, and Cluster 4 (cyan, 13%) from the eastern continental region. The inset shows the convergence of all clusters over the receptor area. Adapted from Google Earth imagery.

dominated by ammonium-neutralised sulphate and nitrate, and another associated with primary BB (e.g., Lalchandani et al., 2022; Sun et al., 2012). In the present PM_{10} dataset, K is strongly correlated with sulphate and nitrate ($\rho \approx 0.80$) and, to a lesser degree, with levoglucosan ($\rho \approx 0.70$), while its association with ammonium is weaker ($\rho \approx 0.30$). This hierarchical correlation structure likely contributed to the merging of SA and BB markers into a single PMF factor. This suggests that the BB influence is strongly tied to secondary atmospheric processing and thus could reflect an aged, mixed biomass-burning plume rather than purely fresh emissions. Domestic biomass burning activities, including charcoal and firewood use for cooking and household energy, occur in Angola and may contribute to the broader BB aerosol burden in Luanda (Amegah, 2018; Rees et al., 2019). However, at the highly urbanised central sampling site, these emissions are more likely to represent intermittent or background influences rather than the dominant local source of this factor. This is consistent with the Angolan household-energy context, where charcoal and fuelwood use are linked to limited energy alternatives and liquefied petroleum gas (LPG) use may be constrained by cost and supply (IEA, 2006). It is also consistent with evidence from southern Africa showing that household cooking fuel choices vary with residence, electricity access, wealth and affordability, and that households may combine traditional and modern fuels

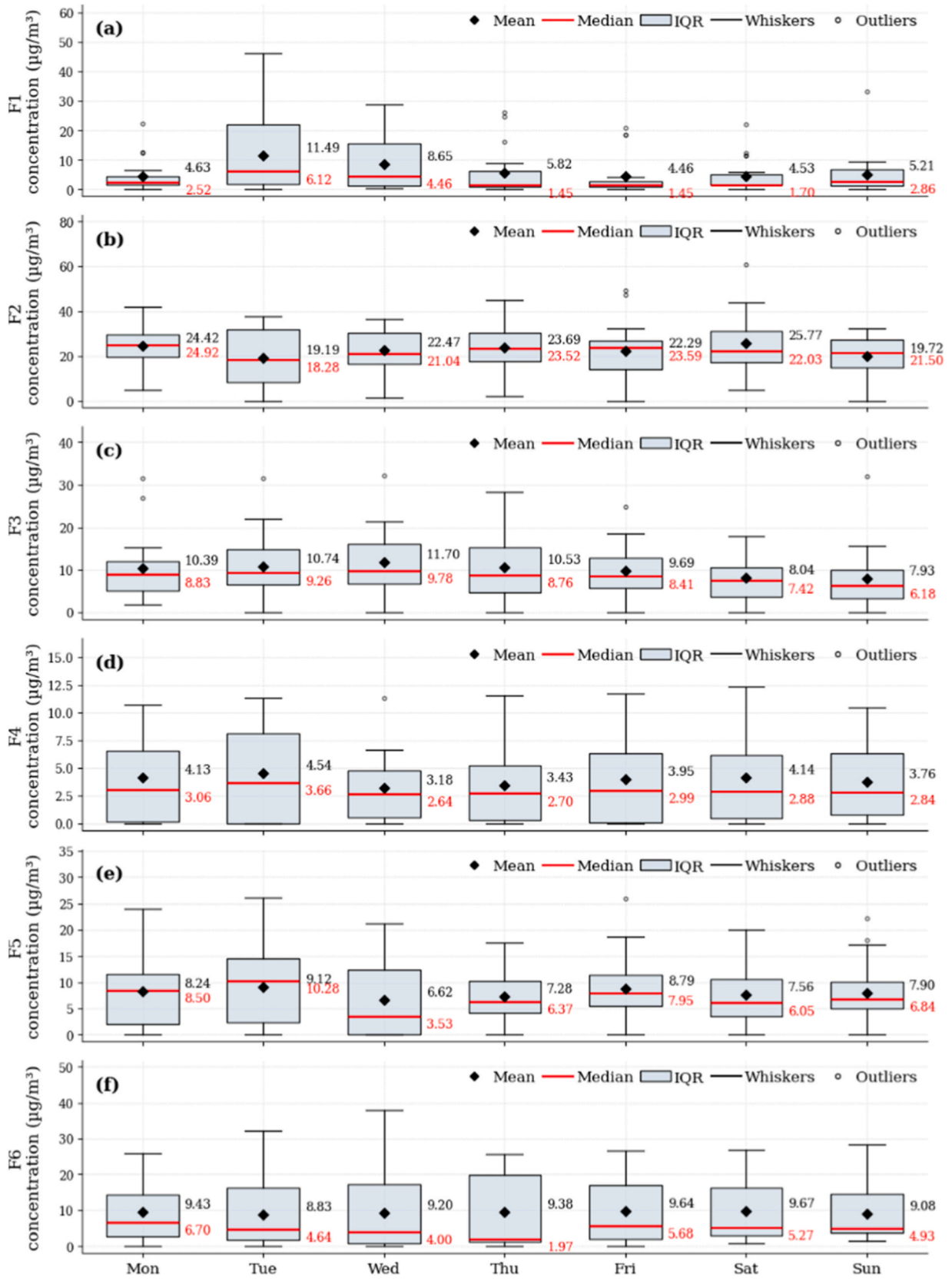

Fig. 6. Day-of-week distributions of mean concentrations for the six PMF-resolved factors at the Luanda sampling site during the PM_{10} campaign. Panels a–f correspond to Factor 1 (non-ferrous metallurgy + galvanised/metal scrap handling and burning), Factor 2 (traffic emissions, exhaust + non-exhaust), Factor 3 (crustal material + resuspended dust), Factor 4 (Ni-rich metallurgical source with local aircraft-related influence), Factor5 (marine crustal aerosol), and Factor 6 (secondary aerosol + biomass burning), respectively.

(Makonese et al., 2018).

Ion balance for this factor reveals an incomplete neutralisation of SA. The neutralisation ratio of 0.38 indicates a deficit of measured ammonium relative to sulphate and nitrate, suggesting that the secondary inorganic aerosol was not fully neutralised, rather than providing a definitive quantification of unneutralised acidic aerosol. This pattern is consistent with, but not diagnostic of, an ammonia-limited regime that could be associated with aqueous-phase SIA formation under high RH conditions. During the campaign, Luanda experienced persistently high relative humidity (80.7 ± 8.33%), a condition that may favour the coexistence of fully neutralised secondary inorganic species [$(NH_4)_2SO_4$ and NH_4NO_3] together with partially neutralised or acidic forms such as ammonium bisulphate [NH_4HSO_4,] (Balasubramanian et al., 2013; Jansen et al., 2014; Young et al., 2022). In humid coastal environments, heterogeneous reactions between [HNO_3] and marine and/or crustal aerosol can promote the formation of sodium and calcium nitrates [$NaNO_3$ and $Ca(NO_3)_2$], thereby enhancing SA formation (Bian et al., 2017; Guo et al., 2019). Part of the apparent ionic imbalance may also reflect the lack of measurements for carbonates and other organic anions, which were not quantified in this study (Balasubramanian et al., 2013).

The factor exhibits an OC/EC ratio of 1.9 (OC: 31.3% of total OC; EC: 17.7% of total EC), a value lower than those typically observed for fresh BB emissions or urban background aerosols – which often range from ~3 to 6 and may exceed 7–10 in BB plumes (Makkonen et al., 2023; Wu et al., 2018). OC/EC ratios above ~2 are frequently interpreted as evidence of a relevant secondary organic carbon (SOC) component (Li et al., 2021), supporting the view that this factor contains a mixture of aged BB and secondary aerosol. The Lev/K ratio (0.13) falls within the lower range reported for crop-residue burning and is markedly below those associated with forest-fire smoke, which typically show much higher values (Wu et al., 2018). The Lev/OC value (0.031) is elevated relative to urban background levels and to some agricultural-burning episodes (e.g., Beijing wheat-straw burning), indicating a non-negligible BB influence (Cheng et al., 2013). These ratios must be interpreted cautiously, as both levoglucosan and OC degrade or volatilise during atmospheric ageing, while K remains comparatively stable. Such processing reduces levoglucosan/OC ratios in transported or mixed plumes (Cheng et al., 2013; Zhang et al., 2024), which is consistent with the aged, regionally influenced character attributed to this mixed SA + BB factor.

During the campaign, NO_2 remained elevated for most of the period, whereas surface O_3 stayed relatively low (14.0 ± 7.6 ppb) and showed a bimodal diurnal cycle, indicating that vertical mixing processes, including convective and residual-layer contributions, were major drivers of surface O_3 variability, rather than local photochemical production being the sole controlling factor (da Silva et al., 2025). The days with the largest contributions from both O_3 and this mixed SA + BB factor coincide with HYSPLIT clusters 1 and 4 (Table 2 & Fig. 5), which transport air masses from southern inland Angola and from the east, crossing neighbouring countries before descending and mixing into the boundary layer over Luanda.

This factor exhibits an apparent seasonal signal (Figs. 4f and 5). Its contribution increases from late June, remaining persistently high through mid-July (25.2 ± 4.9 μg m^{-3}) and culminating in a pronounced peak of 38.1 μg m^{-3} on 20 July. Afterwards, it weakens but remains relevant in August (20.1 ± 3.8 μg m^{-3}), with a secondary sequence of short-lived peaks approaching approximately 26.7 μg m^{-3} on 13 and 19 August. The spatial distribution of active fires detected by MODIS/VIIRS-JPSS (Fig. S7) shows intense fire activity between 13 and 28 July 2023, with a recurrence between 4 and 20 August and several events persisting into late August. When the fire detections are compared with the 120-h HYSPLIT back-trajectories, they help explain the magnitude of the early SA concentrations. The days with the largest contributions from both O_3 and this mixed SA + BB factor coincide with HYSPLIT clusters 1 and 4 (Table 2 & Fig. 5), which transport air masses from southern inland Angola and from the east, crossing neighbouring countries before descending and mixing into the boundary layer over Luanda.

This behaviour is consistent with the broader dry season atmospheric setting in southern Africa, where biomass burning aerosol and terrigenous aerosol are important regional components and where smoke transport is organised by recurrent synoptic scale regimes (Gaetani et al., 2021; Flamant et al., 2024). It is also consistent with an influence of regionally transported biomass burning plumes that undergo chemical processing upwind, remain aloft during transport, and can later mix into the boundary layer, rather than reflecting exclusively local scale formation (Formenti et al., 2018; Dang et al., 2022; Abel et al., 2020). From late August onwards – following the decline in fire activity, which typically influences Luanda's SA burden 2–3 days afterwards – most daily concentrations fall below 5 μg m^{-3}. From mid-September onwards, many values approach or fall below 1 μg m^{-3}, becoming essentially residual by late October–early November. The early-season rise, and subsequent attenuation closely follow the behaviour of the crustal-material factor, which suggests that both were modulated, at least partly, by the same dry season transport conditions favouring regional advection and vertical mixing (Gaetani et al., 2021; Flamant et al., 2024).

4. Conclusions

This study presents the first quantitative PM_{10} source apportionment for the Luanda megacity using the EPA PMF 5.0 receptor model. The numerically stable six-factor solution reveals distinct but interacting emission sources, showing that PM_{10} is largely controlled by local anthropogenic activities and strongly influenced by regional transport and biomass burning plumes. This highlights the coupled role of urban emissions and atmospheric processes in shaping PM_{10} burdens in a coastal megacity. Traffic-related emissions form the dominant class, with the mixed traffic factor (exhaust and non-exhaust) explaining 37.6% of the PM_{10} mass. Industrial and metal-related sources jointly contribute ≈17.2%, partitioned between non-ferrous metallurgy plus galvanised/metal scrap handling and burning (10.8%) and a Ni-centred metallurgical source with an aviation overlay (6.4%). Natural contributions account for a further 29.6%, split into crustal material + resuspended dust (16.5%) and a marine crustal aerosol factor (13.1%). Finally, a mixed secondary aerosol plus biomass-burning factor (SA + BB) explains the remaining 15.5% of the PM_{10} mass, representing a strongly regional and chemically aged contribution.

Despite the robustness of the six-factor solution, some limitations must be acknowledged. The analysis is restricted to a single urban site and a finite sampling period, and the absence of soil dust tracers such as carbonates may partly force secondary inorganic aerosol and biomass burning signatures to merge into a single mixed SA + BB factor. Even so, this first quantitative PM_{10} source apportionment for Luanda provides a coherent picture of the relative contributions of traffic, metal-related industry, crustal dust, marine aerosol and regionally transported biomass burning plumes, and offers a solid platform for future work. Further investigations include extending this approach to longer and multi-site datasets, and linking factor contributions with health-relevant metrics, so that the evidence assembled here can more directly support targeted air quality management in the Luanda megacity.

CRediT authorship contribution statement

Alan Victor da Silva: Data curation, Formal analysis, Investigation, Writing – original draft. **Yago Cipoli:** Formal analysis, Investigation, Methodology. **Estela Vicente:** Formal analysis, Investigation. **Ana Sanchez de la Campa:** Formal analysis, Methodology. **Anabela Leitão:** Resources, Writing – review & editing. **Manuel Feliciano:** Conceptualization, Funding acquisition, Resources, Supervision, Writing – review & editing. **Célia Alves:** Conceptualization, Funding acquisition,

Methodology, Project administration, Resources, Supervision, Writing – review & editing.

Declaration of competing interest

The authors declare that they have no known competing financial interests or personal relationships that could have appeared to influence the work reported in this paper.

Acknowledgments

This work was supported by the Portuguese Foundation for Science and Technology (FCT) through the PhD fellowships 2023.02059. BD, 2023.04826.BD , SFRH/BD/04992/2021 and also for the research contracts under Scientific Employment Stimulus (DOI:10.54499/2022.00399. CEECIND/CP1720/CT0012). The research was performed in the frame of the project APAM, financially supported by national funds (OE), through FCT/MCTES (DOI: 10.54499/2022.04240. PTDC). The financial support to CESAM by FCT/MCTES UID/50006 + LA/P/0094/2020 (doi.org/10.54499/LA/P/0094/2020). This work has also been supported by national funds through FCT/MCTES (PIDDAC): CIMO UID/00690/2025 (10.54499/UID/00690/2025) and UID/PRR/00690/2025 (10.54499/UID/PRR/00690/2025); SusTEC, LA/P/0007/2020 (DOI: 10.54499/LA/P/0007/2020). Additionally, we would like to thank the Faculty of Engineering of the Agostinho Neto University for providing the logistical conditions for carrying out the monitoring campaign in Luanda.

Appendix A. Supplementary data

Supplementary data to this article can be found online at https://doi.org/10.1016/j.apr.2026.103077.

Data availability

Data will be made available on request.

References

Abegglen, M., Brem, B.T., Ellenrieder, M., Durdina, L., Rindlisbacher, T., Wang, J., Lohmann, U., Sierau, B., 2016. Chemical characterization of freshly emitted particulate matter from aircraft exhaust using single particle mass spectrometry. Atmos. Environ. 134, 181–197. https://doi.org/10.1016/j.atmosenv.2016.03.051.

Abel, S.J., Barrett, P.A., Zuidema, P., Zhang, J., Christensen, M., Peers, F., Taylor, J.W., Crawford, I., Bower, K.N., Flynn, M., 2020. Open cells exhibit weaker entrainment of free-tropospheric biomass burning aerosol into the south-east Atlantic boundary layer. Atmos. Chem. Phys. 20, 4059–4084. https://doi.org/10.5194/acp-20-4059-2020.

Alabama Department of Environmental Management - ADEM, 2025. Engineering Analysis: Adanowa Management, LLC – Hot Dip Galvanizing Facility. Chilton County, AL, Montgomery, AL, USA.

Alfeus, A., Molnar, P., Boman, J., Hopke, P.K., Wichmann, J., 2024. $PM_{2.5}$ in cape town, South Africa: chemical characterization and source apportionment using dispersion-normalised positive matrix factorization. Atmos. Pollut. Res. 15, 102025. https://doi.org/10.1016/j.apr.2023.102025.

Alghamdi, M.A., Almazroui, M., Shamy, M., Redal, M.A., Alkhalaf, A.K., Hussein, M.A., Khoder, M.I., 2015. Characterization and elemental composition of atmospheric aerosol loads during springtime dust storm in Western Saudi Arabia. Aerosol Air Qual. Res. 15, 440–453. https://doi.org/10.4209/aaqr.2014.06.0110.

Almeida, S.M., Faria, T., Martins, V., Canha, N., Diapouli, E., Eleftheriadis, K., Manousakas, M.I., 2022. Source apportionment of children daily exposure to particulate matter. Sci. Total Environ. 835, 155349. https://doi.org/10.1016/j.scitotenv.2022.155349.

Alves, C., Vicente, E.D., Nunes, T., Cipoli, Y., Charres, I., Yubero, E., Galindo, N., Ryšavý, J., Leitão, A., 2026. Elemental and carbonaceous composition of PM_{10} and its oxidative potential in schools in Luanda. Atmos. Environ. 364, 121640. https://doi.org/10.1016/j.atmosenv.2025.121640.

Alves, C.A., Feliciano, M.J.S., Gama, C., Vicente, E., Furst, L., Leitão, A., 2024. First exploratory study of gaseous pollutants (NO_2, SO_2, O_3, VOCs and carbonyls) in the Luanda metropolitan area by passive monitoring. Environ. Pollut. 362, 125015. https://doi.org/10.1016/j.envpol.2024.125015.

Alves, C.A., Lopes, D.J., Calvo, A.I., Evtyugina, M., Rocha, S., Nunes, T., 2015. Emissions from light-duty diesel and gasoline in-use vehicles measured on chassis dynamometer test cycles. Aerosol Air Qual. Res. 15, 99–116. https://doi.org/10.4209/aaqr.2014.01.0006.

Alves, C.A., Sanchez de la Campa, A., Cipoli, Y., Furst, L., Higawa, G., Leitão, A., da Silva, A.V., Feliciano, M.S., 2025. PM10-bound elements in Luanda's urban atmosphere: concentrations, sources, and their environmental and health impacts. Environ. Pollut. 372, 125995. https://doi.org/10.1016/j.envpol.2025.125995.

Alves, C.A., Vicente, A.M.P., Calvo, A.I., Baumgardner, D., Amato, F., Querol, X., Pio, C., Gustafsson, M., 2020. Physical and chemical properties of non-exhaust particles generated from wear between pavements and tyres. Atmos. Environ. 224, 117252. https://doi.org/10.1016/j.atmosenv.2019.117252.

Amato, F., Moreno, T., Pandolfi, M., Querol, X., Alastuey, A., Delgado, A., Pedrero, M., Cots, N., 2010. Concentrations, sources and geochemistry of airborne particulate matter at a major European airport. J. Environ. Monit. 12, 854–862. https://doi.org/10.1039/B925439K.

Amegah, A.K., 2018. Proliferation of low-cost sensors. What prospects for air pollution epidemiologic research in Sub-Saharan Africa? Environ. Pollut. 241, 1132–1137. https://doi.org/10.1016/J.ENVPOL.2018.06.044.

Ancelet, T., Davy, P.K., Trompetter, W.J., Markwitz, A., Weatherburn, D.C., 2011. Carbonaceous aerosols in an urban tunnel. Atmos. Environ. 45, 4463–4469. https://doi.org/10.1016/j.atmosenv.2011.05.032.

Balasubramanian, R., Behera, S.N., Betha, R., 2013. Insights into chemical coupling among acidic gases, ammonia and secondary inorganic aerosols. Aerosol Air Qual. Res. 13, 1282–1296. https://doi.org/10.4209/aaqr.2012.11.0328.

Bao, Z., Zhang, X., Li, Q., Zhou, J., Shi, G., Zhou, L., Yang, F., Xie, S., Zhang, D., Zhai, C., Li, Z., Peng, C., Chen, Y., 2023. Measurement report: intensive biomass burning emissions and rapid nitrate formation drive severe haze formation in the sichuan basin, China-insights from aerosol mass spectrometry. Atmos. Chem. Phys. 23, 1147–1167. https://doi.org/10.5194/acp-23-1147-2023.

Becagli, S., Sferlazzo, D.M., Pace, G., Di Sarra, A., Bommarito, C., Calzolai, G., Ghedini, C., Lucarelli, F., Meloni, D., Monteleone, F., Severi, M., Traversi, R., Udisti, R., 2012. Evidence for heavy fuel oil combustion aerosols from chemical analyses at the island of lampedusa: a possible large role of ships emissions in the mediterranean. Atmos. Chem. Phys. 12, 3479–3492. https://doi.org/10.5194/acp-12-3479-2012.

Begum, B.A., Hopke, P.K., 2019. Identification of sources from chemical characterization of fine particulate matter and assessment of ambient air quality in Dhaka, Bangladesh. Aerosol Air Qual. Res. 19, 118–128. https://doi.org/10.4209/aaqr.2017.12.0604.

Benmaamar, M., Arroyo Arroyo, F., Tisso Eduardo, N., 2020. Angola Road Sector Public Expenditure Review, Angola Road Sector Public Expenditure Review. The World Bank Group, Washington, DC. World Bank Publications - Reports 33804.

Bian, H., Chin, M., Hauglustaine, D.A., Schulz, M., Myhre, G., Bauer, S.E., Lund, M.T., Karydis, V.A., Kucsera, T.L., Pan, X., Pozzer, A., Skeie, R.B., Steenrod, S.D., Sudo, K., Tsigaridis, K., Tsimpidi, A.P., Tsyro, S.G., 2017. Investigation of global particulate nitrate from the AeroCom phase III experiment. Atmos. Chem. Phys. 17, 12911–12940. https://doi.org/10.5194/acp-17-12911-2017.

Bozkurt, Z.O., Gaga, E., Taşpınar, F., Arı, A., Pekey, B., Pekey, H., Döğeroğlu, T., Özden Üzmez, Ö., 2018. Atmospheric ambient trace element concentrations of PM_{10} at urban and sub-urban sites: source apportionment and health risk estimation. Environ. Monit. Assess. 190, 168. https://doi.org/10.1007/s10661-018-6517-6.

Brito, J., Rizzo, L.V., Herckes, P., Vasconcellos, P.C., Caumo, S.E.S., Fornaro, A., Ynoue, R.Y., Artaxo, P., Andrade, M.F., 2013. Physical–chemical characterisation of the particulate matter inside two road tunnels in the São Paulo metropolitan area. Atmos. Chem. Phys. 13, 12199–12213. https://doi.org/10.5194/acp-13-12199-2013.

Brown, S.G., Eberly, S., Paatero, P., Norris, G.A., 2015. Methods for estimating uncertainty in PMF solutions: examples with ambient air and water quality data and guidance on reporting PMF results. Sci. Total Environ. 518–519, 626–635. https://doi.org/10.1016/j.scitotenv.2015.01.022.

Campos, P.M.D., Esteves, A.F., Leitão, A.A., Pires, J.C.M., 2021. Design of air quality monitoring network of Luanda, Angola: urban air pollution assessment. Atmos. Pollut. Res. 12, 101128. https://doi.org/10.1016/j.apr.2021.101128.

Carslaw, D.C., Ropkins, K., 2012. Openair - an r package for air quality data analysis. Environ. Model. Software 27–28, 52–61. https://doi.org/10.1016/j.envsoft.2011.09.008.

Caseiro, A., Marr, I.L., Claeys, M., Kasper-Giebl, A., Puxbaum, H., Pio, C.A., 2007. Determination of saccharides in atmospheric aerosol using anion-exchange high-performance liquid chromatography and pulsed-amperometric detection. J. Chromatogr. A 1171, 37–45.

Cavalli, F., Viana, M., Yttri, K.E., Genberg, J., Putaud, J.-P., 2010. Toward a standardised thermal–optical protocol for measuring atmospheric organic and elemental carbon: the EUSAAR protocol. Atmos. Meas. Tech. 3, 79–89. https://doi.org/10.5194/amt-3-79-2010.

Charron, A., Polo-Rehn, L., Besombes, J.L., Golly, B., Buisson, C., Chanut, H., Marchand, N., Guillaud, G., Jaffrezo, J.L., 2019. Identification and quantification of particulate tracers of exhaust and non-exhaust vehicle emissions. Atmos. Chem. Phys. 19, 5187–5207. https://doi.org/10.5194/acp-19-5187-2019.

Chen, J., Hoek, G., 2020. Long-term exposure to PM and all-cause and cause-specific mortality: A systematic review and meta-analysis. Environment International 143, 105974. https://doi.org/10.1016/j.envint.2020.105974. https://linkinghub.elsevier.com/retrieve/pii/S0160412020319292, 105974.

Cheng, Y., Engling, G., He, K.B., Duan, F.K., Ma, Y.L., Du, Z.Y., Liu, J.M., Zheng, M., Weber, R.J., 2013. Biomass burning contribution to beijing aerosol. Atmos. Chem. Phys. 13, 7765–7781. https://doi.org/10.5194/acp-13-7765-2013.

Cipoli, Y.A., Alves, C., Rapuano, M., Evtyugina, M., Rienda, I.C., Kováts, N., Vicente, A., Giardi, F., Furst, L., Nunes, T., Feliciano, M., 2023. Nighttime–daytime PM_{10} source

apportionment and toxicity in a remoteness inland city of the iberian peninsula. Atmos. Environ. 303, 119771. https://doi.org/10.1016/j.atmosenv.2023.119771.
Corral, A.F., Dadashazar, H., Stahl, C., Edwards, E.-L., Zuidema, P., Sorooshian, A., 2020. Source apportionment of aerosol at a coastal site and relationships with precipitation chemistry: a case study over the southeast United States. Atmosphere 11, 1212. https://doi.org/10.3390/atmos11111212.
da Silva, A.V., Furst, L., Cipoli, Y.A., Soares, M.J.S., Leitão, A.G.A., Feliciano, M., Alves, C.A., 2025. First long-term air quality assessment in Luanda, Angola: performance evaluation of a low-cost monitoring station against reference equipment. Atmos. Pollut. Res., 102746 https://doi.org/10.1016/J.APR.2025.102746.
Dang, C., Segal-Rozenhaimer, M., Che, H., Zhang, L., Formenti, P., Taylor, J., Dobracki, A., Purdue, S., Wong, P.-S., Nenes, A., Sedlacek III, A., Coe, H., Redemann, J., Zuidema, P., Howell, S., Haywood, J., 2022. Biomass burning and marine aerosol processing over the southeast Atlantic Ocean: a TEM single-particle analysis. Atmos. Chem. Phys. 22, 9389–9412. https://doi.org/10.5194/acp-22-9389-2022.
Demir, T., Karakaş, D., Yenisoy-Karakaş, S., 2022. Source identification of exhaust and non-exhaust traffic emissions through the elemental carbon fractions and positive matrix factorization method. Environ. Res. 204, 112399. https://doi.org/10.1016/j.envres.2021.112399.
Domingos, J.S.S., Regis, A.C.D., Santos, J.V.S., de Andrade, J.B., da Rocha, G.O., 2012. A comprehensive and suitable method for determining major ions from atmospheric particulate matter matrices. J. Chromatogr. A 1266, 17–23. https://doi.org/10.1016/j.chroma.2012.08.074.
DSEWPaC, 2012. Emission estimation technique manual for galvanizing (version 2.0). Department of Sustainability Environment Water Population and Communities. Canberra, Australia.
Fakhri, N., Stevens, R., Downey, A., Oikonomou, K., Sciare, J., Afif, C., Hayes, P.L., 2024. Source apportionment of $PM_{2.5}$ in Montréal, Canada, and health risk assessment for potentially toxic elements. Atmos. Chem. Phys. 24, 1193–1212. https://doi.org/10.5194/acp-24-1193-2024.
Fisher, S., Bellinger, D.C., Cropper, M.L., Kumar, P., Binagwaho, A., Biao Koudenoukpo, J., Park, Y., Taghian, G., Landrigan, P.J., 2021. Air pollution and development in Africa: impacts on health, the economy and human capital. Lancet Planet. Health 5, e681–e688. https://doi.org/10.1016/s2542-5196(21)00201-1.
Flamant, C., Chaboureau, J.-P., Gaetani, M., Schepanski, K., Formenti, P., 2024. The radiative impact of biomass burning aerosols on dust emissions over Namibia and the long-range transport of smoke observed during the aerosols, radiation and clouds in Southern Africa (AEROCLO-sA) campaign. Atmos. Chem. Phys. 24, 4265–4288. https://doi.org/10.5194/acp-24-4265-2024.
Fomba, K.W., Müller, K., van Pinxteren, D., Poulain, L., van Pinxteren, M., Herrmann, H., 2014. Long-term chemical characterization of tropical and marine aerosols at the cape verde atmospheric observatory (CVAO) from 2007 to 2011. Atmos. Chem. Phys. 14, 8883–8904. https://doi.org/10.5194/acp-14-8883-2014.
Font, A., Tremper, A.H., Priestman, M., Kelly, F.J., Canonaco, F., Prévôt, A.S.H., Green, D.C., 2022. Source attribution and quantification of atmospheric nickel concentrations in an industrial area in the united kingdom (UK). Environ. Pollut. 293, 118432. https://doi.org/10.1016/j.envpol.2021.118432.
Formenti, P., Piketh, S.J., Namwoonde, A., Klopper, D., Burger, R., Cazaunau, M., Feron, A., Gaimoz, C., Broccardo, S., Walton, N., Desboeufs, K., Siour, G., Hanghome, M., Mafwila, S., Omoregie, E., Junkermann, W., Maenhaut, W., 2018. Three years of measurements of light-absorbing aerosols over coastal Namibia: seasonality, origin, and transport. Atmos. Chem. Phys. 18, 17003–17016. https://doi.org/10.5194/acp-18-17003-2018.
Gaetani, M., Pohl, B., Alvarez Castro, M. del C., Flamant, C., Formenti, P., 2021. A weather regime characterisation of winter biomass aerosol transport from Southern Africa. Atmos. Chem. Phys. 21, 16575–16591. https://doi.org/10.5194/acp-21-16575-2021.
Geller, M.D., Ntziachristos, L., Mamakos, A., Samaras, Z., Schmitz, D.A., Froines, J.R., Sioutas, C., 2006. Physicochemical and redox characteristics of particulate matter (PM) emitted from gasoline and diesel passenger cars. Atmos. Environ. 40, 6988–7004. https://doi.org/10.1016/j.atmosenv.2006.06.018.
Gonçalves, C., Alves, C., Vicente, A., Nunes, T., Evtyugina, M., Pio, C., 2021. PM10-Bound sugars: Chemical composition, sources and seasonal variations. Atmosphere 12 (2), 194.
Guo, L., Gu, W., Peng, C., Wang, W., Jie Li, Y., Zong, T., Tang, Y., Wu, Z., Lin, Q., Ge, M., Zhang, G., Hu, M., Bi, X., Wang, X., Tang, M., 2019. A comprehensive study of hygroscopic properties of calcium-and magnesium-containing salts: implication for hygroscopicity of mineral dust and sea salt aerosols. Atmos. Chem. Phys. 19, 2115–2133. https://doi.org/10.5194/acp-19-2115-2019.
HEI, 2025. State of Global Air 2025: a Report on Air Pollution and Its Role in the World's Leading Causes of Death. Health Effects Institute, Boston, MA.
Hopke, P.K., 2010. The application of receptor modeling to air quality data. Pollut. Atmos., n° special 91–110.
Hsu, C.Y., Chi, K.H., Wu, C. Da, Lin, S.L., Hsu, W.C., Tseng, C.C., Chen, M.J., Chen, Y.C., 2021. Integrated analysis of source-specific risks for $PM_{2.5}$-bound metals in urban, suburban, rural, and industrial areas. Environ. Pollut. 275, 116652. https://doi.org/10.1016/j.envpol.2021.116652.
Huang, X.-F., Zou, B.-B., He, L.-Y., Hu, M., Prévôt, A.S.H., Zhang, Y.-H., 2018. Exploration of $PM_{2.5}$ sources on the regional scale in the pearl river Delta based on ME-2 modeling. Atmos. Chem. Phys. 18, 11563–11580. https://doi.org/10.5194/acp-18-11563-2018.
Huntley, B.J., Russo, V., Lages, F., Ferrand, N., 2019. Biodiversity of Angola. Science & Conservation: a Modern Synthesis. Springer Open, Cham, Switzerland. https://doi.org/10.1007/978-3-030-03083-4.
ICH, 2023. ICH Q2(R2): Validation of Analytical Procedures. International Council for Harmonisation. Step 4 guideline, adopted. (Accessed 1 November 2023).
IEA, 2006. Angola: towards an Energy Strategy. International Energy Agency, Paris.
Iinuma, Y., Engling, G., Puxbaum, H., Herrmann, H., 2009. A highly resolved anion-exchange chromatographic method for determination of saccharidic tracers for biomass combustion and primary bio-particles in atmospheric aerosol. Atmos. Environ. 43, 1367–1371. https://doi.org/10.1016/j.atmosenv.2008.11.020.
Jansen, R.C., Shi, Y., Chen, J., Hu, Y.J., Xu, C., Hong, S., Li, J., Zhang, M., 2014. Using hourly measurements to explore the role of secondary inorganic aerosol in $PM_{2.5}$ during haze and fog in hangzhou, China. Adv. Atmos. Sci. 31, 1427–1434. https://doi.org/10.1007/s00376-014-4042-2.
Kara, M., Hopke, P.K., Dumanoglu, Y., Altiok, H., Elbir, T., Odabasi, M., Bayram, A., 2015. Characterization of PM using multiple site data in a heavily industrialized region of Turkey. Aerosol Air Qual. Res. 15, 11–27. https://doi.org/10.4209/aaqr.2014.02.0039.
Kebe, M., Traore, A., Manousakas, M.I., Vasilatou, V., Ndao, A.S., Wague, A., Eleftheriadis, K., 2021. Source apportionment and assessment of air quality index of $PM_{2.5-10}$ and $PM_{2.5}$ in at two different sites in urban background area in Senegal. Atmosphere 12, 182. https://doi.org/10.3390/atmos12020182.
Kelektsoglou, K., Karali, D., Stavridis, A., Loupa, G., 2018. Efficiency of the air-pollution control system of a lead-acid-battery recycling industry. Energies 11. https://doi.org/10.3390/en11123465.
Krittanawong, C., Kamran, Y., Hayes, R.B., Wang, Z., Thurston, G.D., Virani, S., Lavie, C. J., 2023. $PM_{2.5}$ and cardiovascular diseases: state-of-The-art review. Int. J. Cardiol. Cardiovasc. Risk Prev. 19, 200217. https://doi.org/10.1016/j.ijcrp.2023.200217.
Lalchandani, V., Srivastava, D., Dave, J., Mishra, S., Tripathi, N., Shukla, A.K., Sahu, R., Thamban, N.M., Gaddamidi, S., Dixit, K., Ganguly, D., Tiwari, S., Srivastava, A.K., Sahu, L., Rastogi, N., Gargava, P., Tripathi, S.N., 2022. Effect of biomass burning on $PM_{2.5}$ composition and secondary aerosol formation during post-monsoon and winter H-haze episodes in Delhi. J. Geophys. Res. Atmos. 127, 1–21. https://doi.org/10.1029/2021JD035232.
Lee, G., Kim, M., Park, D., Yoo, C., 2023. Fine particulate matter ($PM_{2.5}$) sources and its individual contribution estimation using a positive matrix factorization model. Toxics 11. https://doi.org/10.3390/toxics11010069.
Li, Z., Zhou, R., Li, Y., Chen, M., Wang, Y., Huang, T., Yi, Y., Hou, Z., Meng, J., Yan, L., 2021. Characteristics and sources of organic aerosol markers in $PM_{2.5}$. Aerosol Air Qual. Res. 21. https://doi.org/10.4209/AAQR.210180.
Liu, X., Turner, J.R., Hand, J.L., Schichtel, B.A., Martin, R.V., 2022. A global-scale mineral dust equation. J. Geophys. Res. Atmos. 127, 1–22. https://doi.org/10.1029/2022JD036937.
Liu, X., Zhang, X., Jin, B., Wang, T., Qian, S., Zou, J., Dinh, V.N.T., Jaffrezo, J.-L., Uzu, G., Dominutti, P., Darfeuil, S., Favez, O., Conil, S., Marchand, N., Castillo, S., de la Rosa, J.D., Grange, S., Hueglin, C., Eleftheriadis, K., Manousakas, M.-I., Gini, M., Nava, S., Calzolai, G., Alves, C., Monge, M., Reche, C., Harrison, R.M., Hopke, P.K., Alastuey, A., Querol, X., 2025. Source apportionment of PM_{10} based on offline chemical speciation data at 24 European sites. Clim. Atmos. Sci. 8, 255. https://doi.org/10.1038/s41612-025-01097-7.
Lu, R., Turco, R.P., 1994. Air pollutant transport in a coastal environment. Part I: two-Dimensional simulations of sea-breeza and Mountain effects. J. Atmos. Sci. 51, 2285–2308. https://doi.org/10.1175/1520-0469(1994)051<2285:APTIAC>2.0.CO;2.
Makkonen, U., Vestenius, M., Huy, L.N., Anh, N.T.N., Linh, P.T.V., Thuy, P.T., Phuong, H. T.M., Nguyen, H., Thuy, L.T., Aurela, M., Hellén, H., Loven, K., Kouznetsov, R., Kyllönen, K., Teinilä, K., Kim Oanh, N.T., 2023. Chemical composition and potential sources of $PM_{2.5}$ in hanoi. Atmos. Environ. 299, 119650. https://doi.org/10.1016/j.atmosenv.2023.119650.
Makonese, T., Ifegbesan, A.P., Rampedi, I.T., 2018. Household cooking fuel use patterns and determinants across Southern Africa: evidence from the demographic and health survey data. Energy Environ. 29, 29–48. https://doi.org/10.1177/0958305X17739475.
Malings, C., Westervelt, D.M., Hauryliuk, A., Presto, A.A., Grieshop, A., Bittner, A., Beekmann, M., Subramanian, R., 2020. Application of low-cost fine particulate mass monitors to convert satellite aerosol optical depth to surface concentrations in North America and Africa. Atmos. Meas. Tech. 13, 3873–3892. https://doi.org/10.5194/AMT-13-3873-2020.
Martuzzi, M., Mitis, F., Iavarone, I., Serinelli, M., 2006. Health impact of PM10 and ozone in 13 Italian cities. WHO Regional Office for Europe, Copenhagen, ISBN 9789289022934, p. 133.
Masiol, M., Harrison, R.M., Vu, T.V., Beddows, D.C.S., 2017. Sources of sub-micrometre particles near a major international airport. Atmos. Chem. Phys. 17, 12379–12403. https://doi.org/10.5194/acp-17-12379-2017.
Masiol, M., Harrison, R.M., 2014. Aircraft engine exhaust emissions and other airport-related contributions to ambient air pollution: a review. Atmos. Environ. 95, 409–455. https://doi.org/10.1016/j.atmosenv.2014.05.070.
Massas, I., Gasparatos, D., Ioannou, D., Kalivas, D., 2018. Signs for secondary buildup of heavy metals in soils at the periphery of Athens international airport, Greece. Environ. Sci. Pollut. Res. 25, 658–671. https://doi.org/10.1007/s11356-017-0455-7.
Ministry of Environment of Angola, 2011. National Adaptation Programme of Action Under the United Nations Framework Convention on Climate Change (UNFCCC).
NASA MODIS Science Data Support Team, 2021. MODIS Collection 6.1 NRT Hotspot/Active Fire Detections (MCD14DL) [Data set]. https://doi.org/10.5067/FIRMS/MODIS/MCD14DL.NRT.0061.
NASA VIIRS Land Science Team, 2020. VIIRS NOAA-20 (JPSS-1) 375 m I-Band active fire product NRT (vector data). https://doi.org/10.5067/FIRMS/VIIRS/VJ114IMGT_NRT.002 [Data set].

National Research Council, 1974. Geochemistry and the Environment, Volume I: the Relation of Selected Trace Elements to Health and Disease. National Academies Press, Washington, DC, pp. 51–78. https://doi.org/10.17226/20136.
Norris, G., Duvall, R., Brown, S., Bai, S., 2014. EPA Positive Matrix Factorization (PMF) 5.0 Fundamentals and User Guide. U.S. Environmental Protection Agency, Office of Research and Development, Washington, DC, USA. EPA/600/R-14/108).
Sahel and West Africa Club Secretariat, 2025. Air aware: Building better air quality monitoring in African cities. OECD/SWAC. Paris.
Ogundele, L.T., Owoade, O.K., Olise, F.S., Hopke, P.K., 2016. Source identification and apportionment of $PM_{2.5}$ and $PM_{2.5-10}$ in iron and steel scrap smelting factory environment using PMF, PCFA and UNMIX receptor models. Environ. Monit. Assess. 188, 574. https://doi.org/10.1007/s10661-016-5585-8.
Okuda, T., Nakao, S., Katsuno, M., Tanaka, S., 2007. Source identification of nickel in TSP and $PM_{2.5}$ in Tokyo, Japan. Atmos. Environ. 41, 7642–7648. https://doi.org/10.1016/j.atmosenv.2007.08.050.
Owoade, K.O., Hopke, P.K., Olise, F.S., Ogundele, L.T., Fawole, O.G., Olaniyi, B.H., Jegede, O.O., Ayoola, M.A., Bashiru, M.I., 2015. Chemical compositions and source identification of particulate matter ($PM_{2.5}$ and $PM_{2.5-10}$) from a scrap iron and steel smelting industry along the ife–ibadan highway, Nigeria. Atmos. Pollut. Res. 6, 107–119. https://doi.org/10.5094/APR.2015.013.
Pabroa, P.C.B., Racho, J.M.D., Jagonoy, A.M., Valdez, J.D.G., Bautista VII, A.T., Yee, J. R., Pineda, R., Manlapaz, J., Atanacio, A.J., Coronel, I.C.V., Salvador, C.M.G., Cohen, D.D., 2022. Characterization, source apportionment and associated health risk assessment of respirable air particulates in Metro Manila, Philippines. Atmos. Pollut. Res. 13, 101379. https://doi.org/10.1016/j.apr.2022.101379.
Pereira, G.M., Teinilä, K., Custódio, D., Santos, A.g., Xian, H., Hillamo, R., Alves, C.A., Andrade, J.B., da Rocha, G.O., Kumar, P., Balasubramanian, R., Andrade, M.F., Vasconcellos, P. de C., 2017. Airborne particles in the Brazilian city of São Paulo: one-Year investigation for the chemical composition and source apportionment. Atmos. Chem. Phys. 17, 11943–11969. https://doi.org/10.5194/acp-2017-317.
Pernigotti, D., Belis, C.A., Spanó, L., 2016. SPECIEUROPE: the European data base for PM source profiles. Atmos. Pollut. Res. 7, 307–314. https://doi.org/10.1016/j.apr.2015.10.007.
Pio, C., Cerqueira, M., Harrison, R.M., Nunes, T., Mirante, F., Alves, C., Oliveira, C., Sanchez de la Campa, A., Artíñano, B., Matos, M., 2011. OC/EC ratio observations in Europe: re-thinking the approach for apportionment between primary and secondary organic carbon. Atmos. Environ. 45, 6121–6132. https://doi.org/10.1016/j.atmosenv.2011.08.045.
Querol, X., Alastuey, A., Viana, M., Moreno, T., Reche, C., Minguillón, M.C., Ripoll, A., Pandolfi, M., Amato, F., Karanasiou, A., Pérez, N., Pey, J., Cusack, M., Vázquez, R., Plana, F., Dall'Osto, M., De La Rosa, J., Sánchez De La Campa, A., Fernández-Camacho, R., Rodríguez, S., Pio, C., Alados-Arboledas, L., Titos, G., Artíñano, B., Salvador, P., García Dos Santos, S., Fernández Patier, R., 2013. Variability of carbonaceous aerosols in remote, rural, urban and industrial environments in Spain: implications for air quality policy. Atmos. Chem. Phys. 13, 6185–6206. https://doi.org/10.5194/acp-13-6185-2013.
Ramírez, O., Sánchez de la Campa, A.M., Sánchez-Rodas, D., de la Rosa, J.D., 2020. Hazardous trace elements in thoracic fraction of airborne particulate matter: assessment of temporal variations, sources, and health risks in a megacity. Sci. Total Environ. 710, 136344. https://doi.org/10.1016/j.scitotenv.2019.136344.
Rees, N., Wickham, A., Choi, Y., 2019. Silent suffocation in Africa air pollution is a growing menace. Affecting the Poorest Children the Most. UNICEF, New York.
Rolph, G., Stein, A., Stunder, B., 2017. Real-time environmental applications and display sYstem: ready. Environ. Model. Software 95, 210–228. https://doi.org/10.1016/j.envsoft.2017.06.025.
Sciare, J., Oikonomou, K., Cachier, H., Mihalopoulos, N., Andreae, M.O., Maenhaut, W., Sarda-Estève, R., 2005. Aerosol mass closure and reconstruction of the light scattering coefficient over the eastern Mediterranean Sea during the MINOS campaign. Atmos. Chem. Phys. 5, 2253–2265. https://doi.org/10.5194/acp-5-2253-2005.
Sipkens, T.A., Corbin, J.C., Smith, B., Gagné, S., Lobo, P., Brem, B.T., Johnson, M.P., Smallwood, G.J., 2024. Quantifying the uncertainties in thermal–optical analysis of carbonaceous aircraft engine emissions: an interlaboratory study. Atmos. Meas. Tech. 17, 4291–4302. https://doi.org/10.5194/amt-17-4291-2024.
Soni, A., Kumar, U., Prabhu, V., Shridhar, V., 2019. Characterization, source apportionment and carcinogenic risk assessment of atmospheric particulate matter at dehradun, situated in the foothills of himalayas. J. Atmos. Sol. Terr. Phys. 199, 105205. https://doi.org/10.1016/j.jastp.2020.105205.
Srivastava, D., Xu, J., Vu, T.V., Liu, D., Li, L., Fu, P., Hou, S., Palmerola, N.M., Shi, Z., Harrison, R.M., 2021. Insight into $PM_{2.5}$ sources by applying positive matrix factorization (PMF) at urban and rural sites of beijing. Atmos. Chem. Phys. 21, 14703–14724. https://doi.org/10.5194/acp-21-14703-2021.
Stein, A.F., Draxler, R.R., Rolph, G.D., Stunder, B.J.B., Cohen, M.D., Ngan, F., 2015. Noaa's hysplit atmospheric transport and dispersion modeling system. Bull. Am. Meteorol. Soc. 96, 2059–2077. https://doi.org/10.1175/BAMS-D-14-00110.1.
Su, B., Wang, T., Zhang, G., Liang, Y., Lv, C., Hu, Y., Li, L., Zhou, Z., Wang, X., Bi, X., 2022. A review of atmospheric aging of sea spray aerosols: potential factors affecting chloride depletion. Atmos. Environ. 290, 119365. https://doi.org/10.1016/j.atmosenv.2022.119365.
Sun, Y.L., Zhang, Q., Schwab, J.J., Yang, T., Ng, N.L., Demerjian, K.L., 2012. Factor analysis of combined organic and inorganic aerosol mass spectra from high resolution aerosol mass spectrometer measurements. Atmos. Chem. Phys. 12, 8537–8551. https://doi.org/10.5194/acp-12-8537-2012.
Tao, J., Zhang, L., Zhang, R., Wu, Y., Zhang, Z., Zhang, X., Tang, Y., Cao, J., Zhang, Y., 2016. Uncertainty assessment of source attribution of $PM_{2.5}$ and its water-soluble organic carbon content using different biomass burning tracers in positive matrix factorization analysis - a case study in beijing, China. Sci. Total Environ. 543, 326–335. https://doi.org/10.1016/j.scitotenv.2015.11.057.
Turgut, E.T., Gaga, E.O., Jovanović, G., Odabasi, M., Artun, G., Ari, A., Urošević, M.A., 2019. Elemental characterization of general aviation aircraft emissions using moss bags. Environ. Sci. Pollut. Res. 26, 26925–26938. https://doi.org/10.1007/s11356-019-05910-8.
U.S. EPA, 2017. Definition and Procedure for the Determination of the Method Detection Limit – Revision 2. Appendix B to 40 CFR Part 136. U.S. Environmental Protection Agency.
U.S. EPA, 2020. Epa's Data and Analysis of piston-engine Aircraft Emissions of Lead at U. S. Airports. U.S. Environmental Protection Agency, Washington, DC.
U.S. EPA, 2023. Regulations for Lead Emissions from Aircraft. https://www.epa.gov/regulations-emissions-vehicles-and-engines/regulations-lead-emissions-aircraft.
Viana, M., Amato, F., Alastuey, A., Querol, X., Moreno, T., García Dos Santos, S., Herce, M.D., Fernández-Patier, R., 2009. Chemical tracers of particulate emissions from commercial shipping. Environ. Sci. Technol. 43, 7472–7477. https://doi.org/10.1021/es901558t.
Wang, Z., Hong, N., Chen, Y., Cheng, G., Liu, A., Huang, X., Tan, Q., 2025. Systematic evaluations of receptor models in source apportionment of particulate solids in road deposited sediments: a practical application for tracking heavy metal sources on urban road surfaces. J. Hazard. Mater. 485, 136912. https://doi.org/10.1016/j.jhazmat.2024.136912.
Wu, X., Vu, T.V., Shi, Z., Harrison, R.M., Liu, D., Cen, K., 2018. Characterization and source apportionment of carbonaceous $PM_{2.5}$ particles in China - a review. Atmos. Environ. 189, 187–212. https://doi.org/10.1016/j.atmosenv.2018.06.025.
Young, L.H., Hsiao, T.C., Griffith, S.M., Huang, Y.H., Hsieh, H.G., Lin, T.H., Tsay, S.C., Lin, Y.J., Lai, K.L., Lin, N.H., Lin, W.Y., 2022. Secondary inorganic aerosol chemistry and its impact on atmospheric visibility over an ammonia-rich urban area in central Taiwan. Environ. Pollut. 312, 119951. https://doi.org/10.1016/j.envpol.2022.119951.
Yu, P., Xu, R., Li, S., Coelho, M.S.Z.S., Saldiva, P.H.N., Sim, M.R., Abramson, M.J., Guo, Y., 2022. Loss of life expectancy from $PM_{2.5}$ in Brazil: a national study from 2010 to 2018. Environ. Int. 166, 107350. https://doi.org/10.1016/J.ENVINT.2022.107350.
Zhang, J., Zuend, A., Top, J., Surdu, M., Ei Haddad, I., Slowik, J.G., Prevot, A.S.H., Bell, D.M., 2024. Estimation of the volatility and apparent activity coefficient of levoglucosan in wood-burning organic aerosols. Environ. Sci. Technol. Lett. 11, 1214–1219. https://doi.org/10.1021/acs.estlett.4c00608.
Zhang, X., Hecobian, A., Zheng, M., Frank, N.H., Weber, R.J., 2010. Biomass burning impact on $PM_{2.5}$ over the southeastern US during 2007: integrating chemically speciated FRM filter measurements, MODIS fire counts and PMF analysis. Atmos. Chem. Phys. 10, 6839–6853. https://doi.org/10.5194/acp-10-6839-2010.
Zhao, Y., Yang, X., Du, Y., Chen, L., Dong, J., Hu, T., 2025. Global cardiovascular disease burden attributable to particulate matter pollution, 1990 – 2021: an analysis of the global burden of disease study 2021 and forecast to 2045. BMC Cardiovasc. Disord. 25.
Zheng, X.Y., Guo, S.J., Hu, J.X., Meng, R.L., Xu, Y.J., Lv, Y.H., Wang, Y., Xiao, N., Li, C., Xu, X.J., Zhao, D.J., Zhou, H.Y., He, J.H., Tan, X.M., Wei, J., Lin, L.F., Guan, W.J., 2024. Long-term associations of PM_1 versus $PM_{2.5}$ and PM_{10} with asthma and asthma-related respiratory symptoms in the middle-aged and elderly population. ERJ Open Res 10. https://doi.org/10.1183/23120541.00972-2023.
Zhou, S., Xu, Z., Chen, Y., Zhao, M., Li, Y., Yan, K., 2025. Anthropogenic air pollutants strongly interact with natural aerosols over the eastern China seas: key processes, size distributions, and seasonalities. Atmos. Chem. Phys. 25, 13597–13619. https://doi.org/10.5194/acp-25-13597-2025.